Physics of the Earth and Planetary Interiors 262 (2017) 48–65

Contents lists available at ScienceDirect

Physics of the Earth and Planetary Interiors

journal homepage: www.elsevier.com/locate/pepi

# A probabilistic framework for single-station location of seismicity on Earth and Mars

M. Böse [a,b,*], J.F. Clinton [b], S. Ceylan [a], F. Euchner [a], M. van Driel [a], A. Khan [a], D. Giardini [a], P. Lognonné [c], W.B. Banerdt [d]

[a] Institute of Geophysics, ETH Zurich, Switzerland
[b] Swiss Seismological Service, ETH Zurich, Switzerland
[c] Institute de Physique du Globe de Paris, Paris, France
[d] Jet Propulsion Laboratory, California Institute of Technology, Pasadena, USA

ARTICLE INFO

*Article history:*
Received 13 June 2016
Received in revised form 10 November 2016
Accepted 14 November 2016
Available online 17 November 2016

*Keywords:*
Mars
Earth
Waveforms
Marsquakes
Earthquakes
Location
Surface waves
Body-waves
Travel times

ABSTRACT

Locating the source of seismic energy from a single three-component seismic station is associated with large uncertainties, originating from challenges in identifying seismic phases, as well as inevitable pick and model uncertainties. The challenge is even higher for planets such as Mars, where interior structure is *a priori* largely unknown. In this study, we address the single-station location problem by developing a probabilistic framework that combines location estimates from multiple algorithms to estimate the probability density function (PDF) for epicentral distance, back azimuth, and origin time. Each algorithm uses independent and complementary information in the seismic signals. Together, the algorithms allow locating seismicity ranging from local to teleseismic quakes. Distances and origin times of large regional and teleseismic events ($M > 5.5$) are estimated from observed and theoretical body- and multi-orbit surface-wave travel times. The latter are picked from the maxima in the waveform envelopes in various frequency bands. For smaller events at local and regional distances, only first arrival picks of body waves are used, possibly in combination with fundamental Rayleigh *R1* waveform maxima where detectable; depth phases, such as *pP* or *PmP*, help constrain source depth and improve distance estimates. Back azimuth is determined from the polarization of the Rayleigh- and/or *P*-wave phases. When seismic signals are good enough for multiple approaches to be used, estimates from the various methods are combined through the product of their PDFs, resulting in an improved event location and reduced uncertainty range estimate compared to the results obtained from each algorithm independently. To verify our approach, we use both earthquake recordings from existing Earth stations and synthetic Martian seismograms. The Mars synthetics are generated with a full-waveform scheme (AxiSEM) using spherically-symmetric seismic velocity, density and attenuation models of Mars that incorporate existing knowledge of Mars internal structure, and include expected ambient and instrumental noise. While our probabilistic framework is developed mainly for application to Mars in the context of the upcoming InSight mission, it is also relevant for locating seismic events on Earth in regions with sparse instrumentation.



## 1. Introduction

Mars' interior is expected to still reflect the differentiation and early planetary formation processes that have been lost on Earth due to mantle convection (Solomon et al., 2005). Investigating the interior structure of Mars has therefore been a high-priority objective for planetary scientists since the Viking missions in the mid-1970s (Anderson et al., 1977). NASA supports the scientific discovery and exploration of Mars with multiple programs, including the InSight (**In**terior exploration using **S**eismic **I**nvestigations, **G**eodesy and **H**eat **T**ransport) Discovery Program mission. InSight will deploy a lander equipped with geophysical, geodetic, and meteorological sensors on the Martian surface (Banerdt et al., 2013), including a single three-component ultra-sensitive very-broadband seismometer (VBB; Lognonné et al., 2012; Mimoun et al., 2012). InSight mission goals include (1) providing one-dimensional models of Mars' mantle and core to within ±5% uncertainty in seismic wave-speeds, as well as three-dimensional velocity models of the crust; and (2) measuring the activity and distribution of seismic events on Mars, including both tectonic

* Corresponding author at: ETH Zurich, Sonneggstr. 5, 8092 Zurich, Switzerland.
*E-mail address:* mboese@sed.ethz.ch (M. Böse).

http://dx.doi.org/10.1016/j.pepi.2016.11.003
0031-9201/

and impact seismicity (Banerdt et al., 2013). The InSight launch is targeted for May 2018.

The detection and characterisation of seismicity is important to understand the tectonic and possible volcanic activity of a planet. In this study, we develop and verify methods for single-station event-location for local, regional, and teleseismic seismicity on Earth and Mars. To deal with the inevitably large uncertainties associated with these event parameters from a single station, we develop a probabilistic framework, which accounts for both observation and model uncertainties. Aside from characterizing Martian seismicity for InSight and similar future planetary missions, single-station methods have terrestrial applications (Frohlich and Pulliam, 1999), such as for seismic and nuclear (CTBTO) monitoring, particularly in regions with sparse instrumentation or in countries that operate small seismic networks or single stations only (e.g., Agius and Galea, 2011). Single-station methods are also relevant to earthquake early warning (e.g., Kanamori, 2005; Böse et al., 2012).

Seismic data from InSight will become available in early 2019. To verify our event location approach we use both seismic records from stations on Earth and synthetic Martian seismograms. The latter are computed from a full-waveform scheme (AxiSEM; Nissen-Meyer et al., 2014; van Driel et al., 2015) using spherically-symmetric seismic velocity and density models that incorporate existing knowledge on the internal structure of Mars, as well as predicted ambient and instrumental noise characteristics (Murdoch et al., 2015a,b). In this paper we present a novel approach to single-station location. In our companion paper, Khan et al. (2016), we apply this method to marsquake simulations, and extend the approach to simultaneously invert for structure.

### 1.1. Seismic activity on Mars

Seismic activity on Mars is anticipated to be similar to terrestrial intraplate activity (Anderson et al., 1972, 1977) with a total moment release in-between that of the Earth and Moon (Golombek et al., 1992). Theoretical models for thermo-elastic cooling (Phillips, 1991) and observed surface faults (Golombek et al., 1992; Knapmeyer et al., 2006) predict a Martian annual occurrence of ~50 globally detectable marsquakes with seismic moments of $\sim 10^{15}$ Nm ($\sim m_b = 4$), and ~5–10 times more quakes for each unit decrease in moment magnitude (Golombek, 2002).

Without plate tectonics on Mars, we expect that secular cooling of the planet as described in Phillips (1991) is the driver of sustainable tectonic stress. Independent of this, another source of seismic events on Mars are meteorite impacts, that are expected to constitute ~20% of all observed events, similar to observations on the Moon (Banerdt et al., 2013). The Apollo 14 seismometer detected on the Moon about 100 events per year with ground velocities $>10^{-9}$m/s (Oberst and Nakamura, 1991; Lognonné et al., 2009). The larger mass of Mars suggests 2–4 times more impacts (Banerdt et al., 2013), although the velocity of these impacts will only be half due to smaller orbital velocities and to the additional deceleration in the atmosphere of Mars, which is absent on the Moon (Lognonné and Johnson, 2007, 2015; Lognonné and Kawamura, 2015). In a recent study, however, Teanby and Wookey (2011) find that detectable impacts at teleseismic distances of >60° are likely going to be rare and may occur only once every 10 years; local impacts, on the other hand, are expected to be more frequently detectable. Successful identification and location of meteorite impacts is crucially important to produce ground truth locations that will strongly constrain structural models of Mars. Approximate locations of suspected meteorite impacts will be used as targets for gathering high-resolution orbital images, in order to visually identify and provide exact impact locations. Even though we presently focus on the location problem for marsquakes, we expect our approach to be applicable to locate impacts, provided that at least two seismic phases can be identified.

## 2. Method

Seismic (point-) source locations are commonly characterized by four parameters: (1) latitude $\varphi$, (2) longitude $\lambda$, (3) depth $h$, and (4) origin time $t_0$. In single-station processing, the problem is often decomposed: absolute event locations ($\varphi$, $\lambda$) are replaced by epicentral distances $\Delta$ and back azimuths $\Theta$ *relative* to the single station (e.g., Frohlich and Pulliam, 1999; Magotra et al., 1987). The advantage of this decomposition is that $\Delta$ and $\Theta$ can be determined independently of each other and be combined at a subsequent stage to provide an absolute event location ($\varphi$, $\lambda$). With the resulting location, $t_0$ can then be easily computed from available velocity models.

Estimating the source depth from a single sensor is challenging. Certain secondary phases, such as *PmP*, *SmP*, *pP* or *sP*, are depth-sensitive and if identifiable could potentially be used to infer $h$. Similarly, cross-correlation techniques or relative amplitudes of body-to-surface wave energy are useful. Though in this study we mainly focus on determining $\Delta$, $t_0$ and $\Theta$, we will illustrate how depth can be determined from *PmP* or *pP* using the examples of two small local quakes on Earth and Mars.

Single-station locations, as a matter of principle, are associated with large inherent uncertainties that originate from inevitable pick and model uncertainties (e.g. Husen and Hardebeck, 2010), and potential mis-identification of seismic phases. In this study, we address the problem of single-station event location in a probabilistic framework that combines multiple algorithms with the goal to estimate the probability density functions (PDFs), $p(\Delta)$, $p(t_0)$, and $p(\Theta)$, for observing $\Delta$, $t_0$ and $\Theta$ given a set of observed phase picks (and uncertainties) and the polarization of surface and body waves.

In the following sections, we present two single-station algorithms to estimate $p(\Delta)$ [and $p(t_0)$] from picks of seismic phase arrivals, and two algorithms to estimate $p(\Theta)$ from wave polarization. We demonstrate that event location estimates improve significantly through the combination of multiple algorithms, which mathematically corresponds to a multiplication of the respective PDFs:

$$P(X) \propto \prod_M p_M(X), \quad X = \{\Delta, \Theta, t_0\}, \tag{1}$$

where M is the method used. The procedure is schematically illustrated in Fig. 1.

### 2.1. Distance estimation from multi-orbit Rayleigh-waves: $p_{R1\ R2\ R3}(\Delta)$

Rayleigh waves propagate along the free surface of a planet and are characterized by elliptical ground-motions. Their amplitudes decay slower with increasing distance than those of seismic body waves, which spread out in three dimensions from the source. Therefore, Rayleigh waves are typically detectable at much larger hypocentral distances than body waves. Large events may generate Rayleigh waves that travel multiple times around the whole globe before their amplitudes are attenuated below the level of background noise. The first 3 multi-orbit phase arrivals are named *R1*, *R2*, and *R3*, where *R1* propagates along the minor-arc from the quake towards the receiver; *R2* takes the opposite direction around the planet along the major arc; *R3* propagates along the minor arc plus another trip around the great circle path.

Differential times between multi-orbit Rayleigh-wave phase-arrivals can be used to infer epicentral distance $\Delta$ and origin time

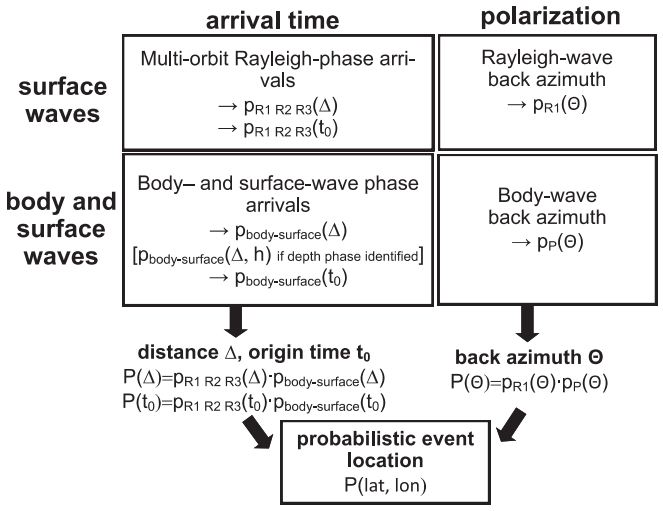


**Fig. 1.** Illustration of the location approach using a single station. The absolute event location and its uncertainty are determined from epicentral distance Δ and back azimuth Θ (relative to the receiver), which are probabilistically estimated from phase picks and the polarization of surface and body waves. Depth phases, if identified, constrain the event depth *h*. The combination of multiple approaches that are based on complementary information contained in body and surface waves adds robustness to the overall solution. See main text for more details.

$t_0$ (The alternative usage of Love waves is discussed in Section 5). Since Rayleigh waves are dispersive, *R1*, *R2*, and *R3* (group-) arrival times $t_{R1}$, $t_{R2}$, and $t_{R3}$ are frequency-dependent. Following Panning et al. (2015), we filter the vertical component of a given broadband seismogram in a series of $N_b$ band-pass 1/2 octave-wide filters using a second-order Butterworth filter with 20% frequency band overlap. The frequency range, where Rayleigh waves are visible above the background noise, does not only depend on the magnitude and distance to the station, but also on the typical noise of the station which is strongly limited by the planet (see Section 3). We pick $t_{R1_b}$, $t_{R2_b}$, and $t_{R3_b}$ from the peak energy of the corresponding waveform envelope in each frequency band *b* provided that the signal-to-noise ratio SNR >1.5 (where the per-band noise amplitudes are determined over a pre-event time window of 30 min). The epicentral distance $\Delta_b$ and origin time $t_{0_b}$ are then determined from

$$\Delta_b = \pi - \frac{1}{2} U_b (t_{R2_b} - t_{R1_b}) \tag{2.1}$$

$$t_{0_b} = t_{R1_b} - \frac{\Delta_b}{U_b} \tag{2.2}$$

where the angular group velocity $U_b$ is given by

$$U_b = \frac{2\pi}{t_{R3_b} - t_{R1_b}} \tag{2.3}$$

where $\Delta_b$ is in radians and $U_b$ in radians/s.

For application to less favorable conditions, in which *R1*, *R2*, and *R3* cannot be clearly identified, because of multiple peaks in the waveform envelopes produced by noise sources with similar or greater amplitudes than the Rayleigh wave trains or by multipathing (see Fig. 2b for example), we modify the original algorithm to accept different pick combinations and thus multiple solutions for $\Delta_b$ and $t_{0_b}$, each weighted by the amplitudes and group-velocities of their picked Rayleigh-wave arrivals. That is, instead of picking $t_{R1_b}$, $t_{R2_b}$, and $t_{R3_b}$, we consider all $i = 1 \ldots N_i$ peak-combinations with pick times $t^{(i)}_{R1_b}$, $t^{(i)}_{R2_b}$, and $t^{(i)}_{R3_b}$, assuming that $t^{(i)}_{R1_b} > t^{(i)}_{R2_b} > t^{(i)}_{R3_b}$. Each combination provides an independent set of parameter estimates $\Delta^{(i)}_b$, $t^{(i)}_{0_b}$, and $U^{(i)}_b$, which can be determined from Eqs. (2.1)–(2.3). The final PDF $p_{R1\ R2\ R3}(X)$ with $X = \{\Delta, t_0\}$ is obtained from summing up the PDFs of all amplitude- and velocity-weighted solutions. Details of this approach are given in the Appendix A.

Note that the approach described above does not require any prior velocity model, which is particularly intriguing for application to Mars, since the interior structure is largely unknown. Overall, this method is well-suited for estimating epicentral distances and origin times of quakes with clearly identifiable *R1*, *R2*, and *R3* arrivals in at least some of the band-passes. In particular, a strong *R1* phase is required to predict and recognize the later *R3* arrival. On Earth this is generally true for larger quakes ($M \geqslant 6$) located at distances $10 < \Delta < 170^o$ that are far enough away from the station and the antipode where phases are not well-separated (see discussion in Section 5).

### 2.2. Distance estimation from body- and surface-wave phase-arrivals: $p_{body\text{-}surface}(\Delta)$

Seismic body waves travel through the planetary interior and are therefore strongly affected by the seismic velocities in the crust, mantle, and core. Unlike in the Rayleigh-wave approach (Section 2.1), in which *a priori* structure is not required (though the computed Rayleigh wave group velocities can be used to invert for structure as shown in our companion paper Khan et al. (2016)), inferring quake locations from body-phase arrivals requires models of interior structure.

While global one-dimensional (e.g., iasp91: Kennett and Engdahl, 1991; prem: Dziewonski and Anderson, 1981; ak135: Kennett et al., 1995) and three-dimensional models (see Dziewonski and Romanowicz (2007) for review) for Earth exist, only few constraints exist on the interior structure of Mars (e.g., Khan and Connolly, 2008; Rivoldini et al., 2011; Verhoeven et al., 2005; Zharkov and Gudkova, 2005; Nimmo and Faul, 2013; Mocquet and Menvielle, 2000; Sohl and Spohn, 1997). Sets or families of periodically updated one-dimensional structure models of the mantle and core, as well as three-dimensional models of the crust, will be derived and iteratively refined from the seismic and geodetic observations during the InSight mission (Banerdt et al., 2013).

Aside from these model uncertainties, the practice of picking seismic phase arrivals in the seismogram does include an additional source of uncertainty (e.g. Husen and Hardebeck, 2010), even when these phases can be correctly identified. The timing of a manual phase pick can often differ from analyst to analyst by up to several seconds, and often depends on filtering and application of other data pre-processing steps (Diehl et al., 2011). This problem is even more severe in environments with significant site noise or in the presence of highly scattering media, such as on the Moon (e.g. Lognonné et al., 2003; Nakamura, 2005), for which errors in the timing as large as 10 s can be found, especially on *S* waves; probabilistic determination of the Lunar Quake and Impacts location has therefore been used by Khan and Mosegaard (2002) and Gagnepain-Beyneix et al. (2006). A similar situation may be also encountered on Mars.

To estimate the epicentral distance and origin time of a seismic event from phase arrivals, we propose a method that takes the uncertainties in both models and picks into account. Here we focus on body-wave phases, but demonstrate that this approach can be extended to frequency limited peak phase arrivals for surface waves, such as *R1* filtered between 120 and 180 s. Our approach requires arrival times $\{t^{obs}_{phase}\}$ of at least $N_{picks} = 2$ identified (e.g. *P*, *S*, *R1@120–180s*) phases. Each pick is assumed to have an

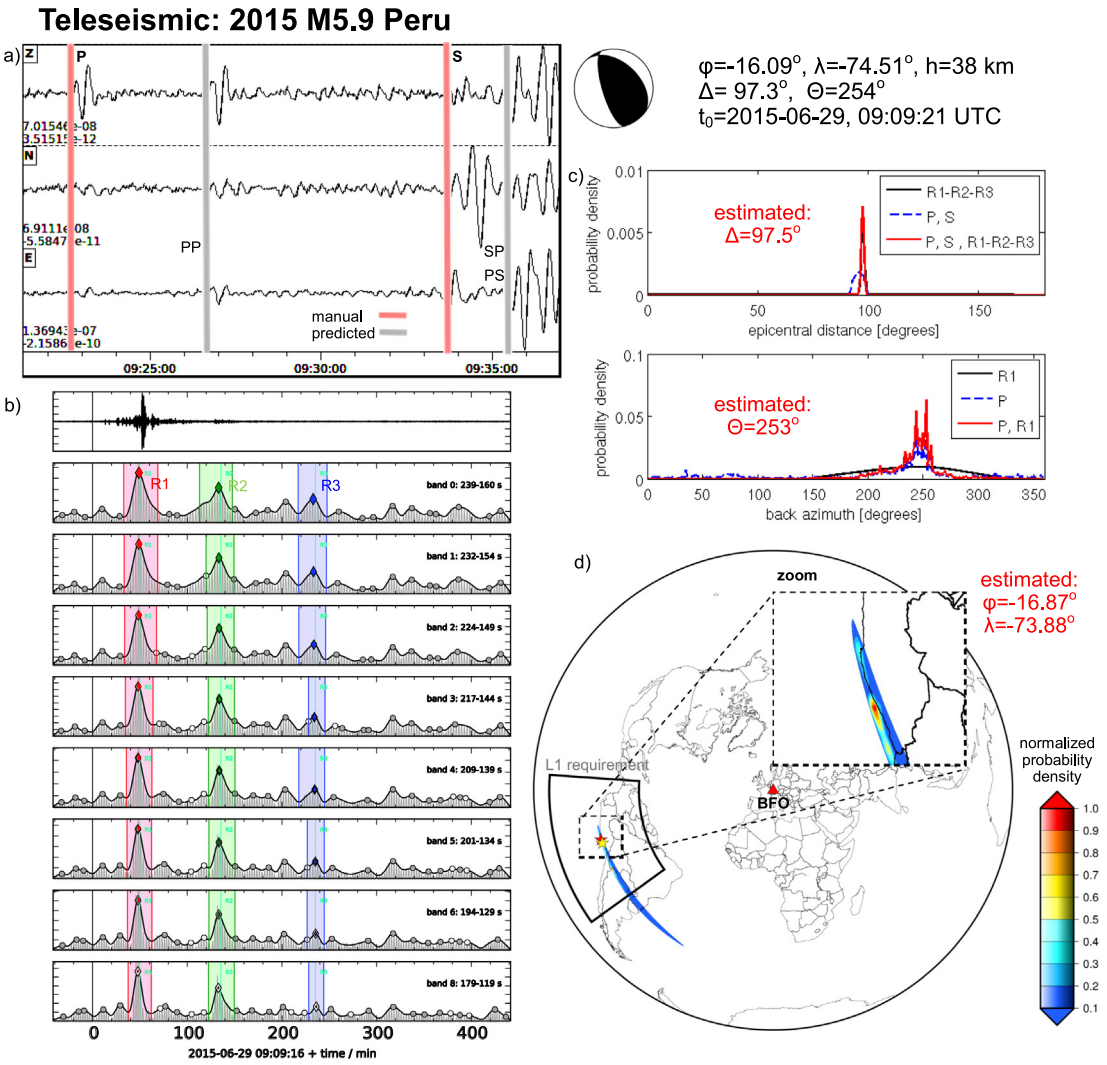


**Fig. 2.** Building a single-station probabilistic location for a moderate-sized M5.9 earthquake at ~97° (teleseismic) distance from station BFO. a) Three-component seismogram at BFO with manually picked *P*- and *S*-wave arrivals (red; see Table 1 for details); secondary *pP* and *SP*/*PS* arrivals (gray) are predicted from the distance estimated from our approach; these arrivals are not used here to locate the event. b) Broadband seismogram and waveform envelopes of vertical component filtered in 9 frequency bands between 120 and 240 s. Red, green and blue dots show automatically picked *R1*, *R2*, and *R3* arrivals (and time windows) with largest amplitudes and expected group velocities; cyan lines show theoretical arrivals. Other arrival candidates (gray dots) are considered in the probabilistic location approach as well, but reach low probabilities only. c) Probability density functions (PDFs) for epicentral distance (top) and back azimuth (bottom) using the picks and polarization of Rayleigh- and body-waves or the combination of both. Red lines show combined PDFs obtained from multiplication of results from the different methods. d) Catalogue (red star) and estimated single station event location (yellow star) and color-coded uncertainty range using azimuthal equidistant map projection. The estimated location meets the L1 requirements of the InSight mission (black line). See Table 1 for details. (For interpretation of the references to colour in this figure legend, the reader is referred to the web version of this article.)

uncertainty $\sigma^{obs}_{phase}$, which can be modeled, for instance, by a uniform distribution

$$f^{obs}_{phase}(t) = \begin{cases} \frac{1}{\sigma^{obs}_{phase}} & \text{for } t \epsilon [t^{obs}_{phase} - 0.5\sigma^{obs}_{phase}, t^{obs}_{phase} + 0.5\sigma^{obs}_{phase}] \\ 0 & \text{otherwise} \end{cases} \quad (3.1)$$

In practice, the uncertainty is defined by the data analyst, who, as well as selecting the most likely phase arrival time, also selects a window indicating the earliest and latest possible arrival times for that phase. Since the event origin time $t_0$ is typically unknown, we use differential times $t^{obs}_{phase-ref}$ relative to a picked (reference) phase arrival, for instance relative to *P*, and determine the corresponding probability density function $f^{obs}_{phase-ref}(t)$ using Eq. (3.1). The reference phase is always defined as the earliest identified phase. The theoretical (differential) phase-arrival times $t^{pred}_{phase-ref,m}(\Delta, h)$ for a given epicentral distance $\Delta$ and focal depth $h$ are predicted from a suite of m = 1...M velocity models. Finally, $f^{pred}_{phase-ref}(t|\Delta, h)$ is computed from the distribution of the predicted differential times using all M models.

To estimate the probability that the event occurred at distance $\Delta$ and source depth $h$, given the phase pick times and their associated uncertainties, we integrate the product of the observed and predicted travel-time distributions over time $t$ and sum this result for all phases identified in addition to the reference phase

$$p_{body-surface}(\Delta, h) \propto \sum_{phase} \int f^{obs}_{phase-ref}(t) f^{pred}_{phase-ref}(t|\Delta, h) dt \quad (3.2)$$

Unless we pick a so-called depth phase, we have no information on $h$. Thus if a depth phase is identified, we use Eq. (3.2), otherwise we integrate over depth $h$ (here from 0 to 600 km) and compute the marginal likelihood as

$$p_{body-surface}(\Delta) \propto \sum_{phase} \int \int f^{obs}_{phase-ref}(t) f^{pred}_{phase-ref}(t|\Delta, h) dt dh \quad (3.3)$$

Once the distance is determined, $p_{body-surface}(t_0)$ is estimated from the available velocity models. As shown later, the described approach can be easily extended to include combinations of body- and surface-wave arrivals, if theoretical models and travel times exist.

This method requires at least 2 clearly identified body phases, or one body phase and one band-passed Rayleigh phase. It can be used for a wide variety of seismic events, as long as impulsive phases are recorded with high signal-to-noise ratio. This means that the approach is appropriate for all sizes of local events, as well as moderate regional and teleseismic events.

### 2.3. Back-azimuth estimation from Rayleigh wave: $p_{R1}(\Theta)$

Rayleigh waves exist at the free surface of a planet as a superposition of vertically polarized *P*- and *SV* motions. Due to the phase shift between the vertical and radial components with a 90° advance of the vertical component, Rayleigh waves exhibit retrograde elliptical particle motions at the planet surface. The back azimuth $\Theta$ can be determined from Rayleigh wave energy at a single sensor either from the eigenvalues and eigenvectors of the $3 \times 3$ covariance matrix from the three-component seismogram (e.g. Selby, 2001), or from the cross-correlation of the radial and vertical components (e.g. Chael, 1997).

In the cross-correlation approach, it is necessary to Hilbert transform the vertical (or radial) component of the seismogram to remove the 90° phase shift, and thus to convert the elliptical polarization of the fundamental mode Rayleigh wave into linear motion (Chael, 1997). The back azimuth $\Theta$ is found from rotating the radial components *r* through various trial angles. For each of these angles, we compute the cross-correlation value $C_{\bar{z}r}$ between *r* and the Hilbert-transformed vertical component $\bar{z}$ to quantify the polarization, where

$$C_{\bar{z}r} = \frac{S_{\bar{z}r}}{S_{\bar{z}\bar{z}} S_{rr}}, \quad \text{where} \quad S_{jk} = \int x_j(t) x_k(t) dt \quad (4.1)$$

The back azimuth is determined from the angle with minimum of $C_{\bar{z}r}$. In practice, the back azimuth is calculated in a manually defined time window that spans the major energy of the *R1* wavetrain selected from the waveform envelopes of the vertical component (see Figs. 3b and 4b for example). The resulting back azimuth depends on the orientation of minimum correlation between the vertical and horizontal components, rather than on the direction of maximum ground-motion, and thus is insensitive to coda of preceding arrivals (such as *S*- or Love waves) that may be included in the *R1* time window (Chael, 1997). Notice that a prominent peak in the correlation function in Eq. (4.1) is often absent, in particular when there is only weak Love wave energy (Panning et al., 2015). In these cases, $\Theta$ cannot be well resolved. Baker and Stevens (2004) suggest using the cross-correlation value $C_{\bar{z}r}$ in Eq. (4.1) as a proxy of the (empirical) accuracy of the back azimuth estimate.

Here, we select the described approach because of its insensitivity towards noise, as well as its lack of 180° ambiguity in the predicted back azimuth, which is typical for body wave-based polarization approaches. Because we are not only interested in the optimum solution for $\Theta$, but $p(\Theta)$, we consider all trial angles and cross-correlation coefficients as defined in Eq. (4.1) above some (arbitrary) threshold, e.g. here we use $C_{\bar{z}r} \geqslant 0$, and model the estimated probability density function as

$$p_{R1}(\Theta) \propto \begin{cases} C_{\bar{z}r}(\Theta), & \text{if} C_{\bar{z}r}(\Theta) \geqslant C_{threshold} \\ 0, & \text{otherwise} \end{cases} \quad (4.2)$$

This approach is similar to data-culling and computation of confidence intervals for determination of OBS sensor orientations described in Stachnik et al. (2012). In practice, we determine the angle-dependent cross-correlation function in each frequency band *b* (see Section 2.1), and then for each trial azimuth average $C_{\bar{z}r}$ over all bands.

This method requires *R1* energy and can be applied to a wide range of events sizes and distances. Errors in azimuth determined from *R1* polarization on Earth are typically in the order of ~30°.

### 2.4. Back-azimuth estimation from body wave: $p_P(\Theta)$

Our second approach for back azimuth ($\Theta$) estimation uses the polarization of seismic body-wave phases. *P*-phases usually provide the best estimates since they are not contaminated by the coda of preceding phases. However, other phases of vertically polarized (*P-SV*) waves could in principle be used as well, while horizontally polarized (*SH*) waves require a different approach. We determine $\Theta$ from the amplitude ratio of the two horizontal components, here denoted traditionally by *e* for East component and *n* for the North component,

$$\theta_i = \begin{cases} \arctan(e_i/n_i) + \pi, & \text{if} z_i n_i < 0 \\ \arctan(e_i/n_i), & \text{otherwise} \end{cases} \quad (5.1)$$

where *i* marks the sample index in the considered time window, *z* the vertical component, and arctan () is the inverse tangent function. Similarly to Eisermann et al. (2015), we resolve the 180° ambiguity in the computed back azimuth from the fact that the back azimuth vector cannot point outside the lower half-space. The resulting flipping condition in Eq. (5.1) is valid for *P* waves and is independent of the source mechanism (Eisermann et al., 2015).

Various approaches have been suggested to identify the optimum body-phase time-window for back azimuth measurement (e.g. Eisermann et al., 2015). Since these approaches have an inherent number of free parameters, in practice it is reasonable to use the distribution of back azimuth values spanning various *P* and *SV* arrivals when available in order to determine $p_P(\Theta)$. In this study, we apply Eq. (5.1) to all samples *i* in a given time interval following the *P*-arrival. Each sample is weighted with $(e_i^2 + n_i^2)$. The length of the time window is determined manually by the data analyst and, by observation, this duration has only a weak impact on $p_P(\Theta)$, as long as *SH* energy is not included.

This method requires *P* or *SV* wave energy, so can also be applied to a wide range of event sizes and distances, in particular small local events.

## 3. Data and synthetic waveforms

To demonstrate and verify our proposed single-station location framework, we use the seismic recordings from three small and moderate-sized quakes at local, regional and teleseismic distances for the Earth, as well as synthetic data for three marsquakes at similar distances (in terms of degrees), but with smaller magnitudes.

### 3.1. Earth

For demonstration on Earth, we use ground motions recorded on the three-component broadband STS-2 velocity sensor at station BFO ($\varphi = 48.33°$, $\lambda = 8.33°$), located in the Black Forest Observatory, Germany. We randomly select three small and moderate-sized earthquakes at teleseismic (2015 M5.9 Peru, $\Delta \approx 97°$), regional (2015 M5.6 Egypt, $\Delta \approx 28°$), and local (2012 M3.7 Switzerland, $\Delta \approx 1.5°$) distances (Table 1). Though seismic phases are usually easier to pick and locations thus better constrained for large events, we want to verify the applicability of our approach to

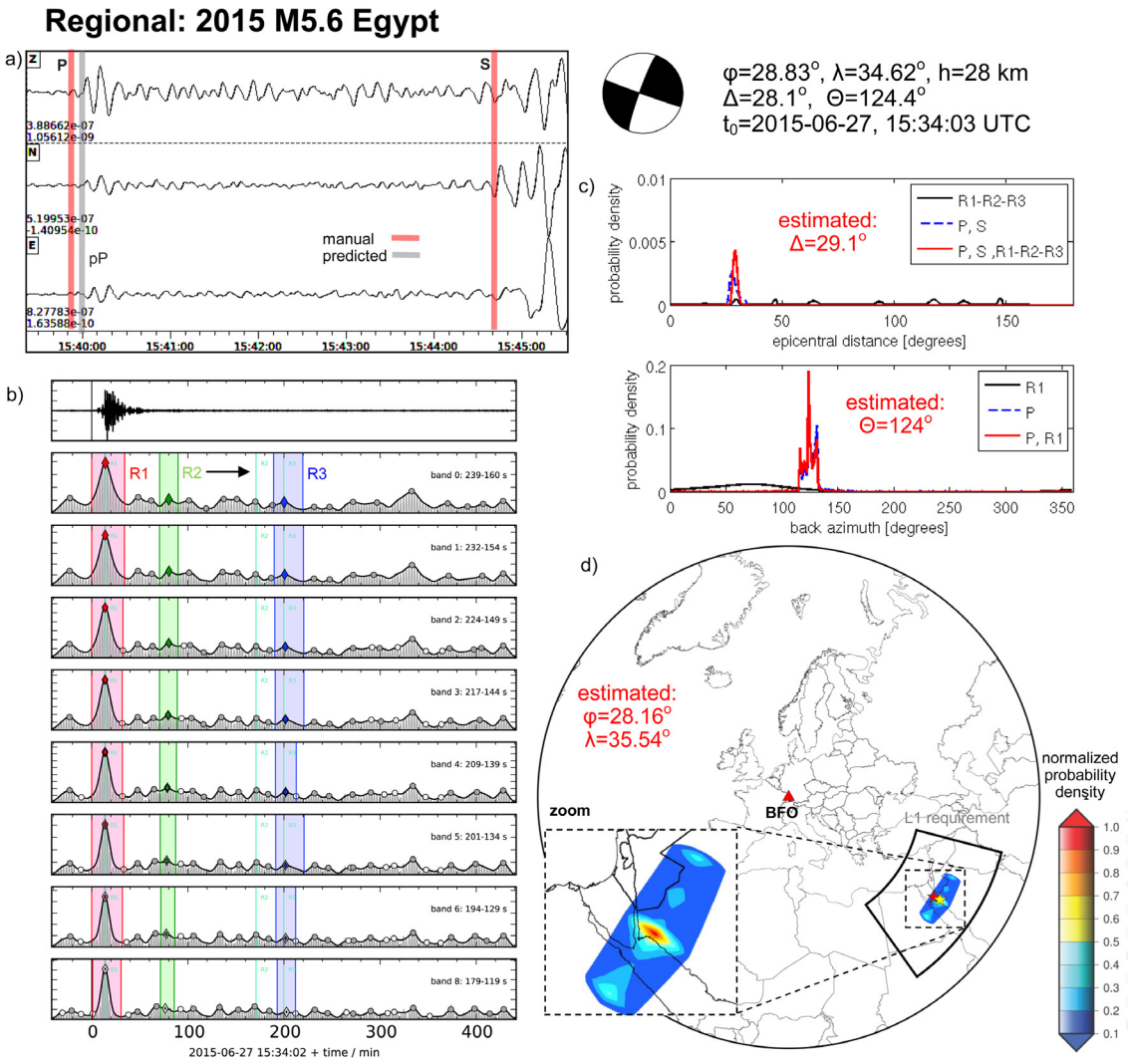


**Fig. 3.** Building a single-station probabilistic location for a moderate-sized M5.6 earthquake at ~28° (regional) distance from station BFO. See caption of Fig. 2 for explanation. Notice that the *R2* picks of the best solution (green) in b) do not agree with the correct arrivals (cyan), because high noise leads to multiple distance solutions with similar probabilities (black line in c, top). A unique and well-defined solution is obtained when the results of Rayleigh- and body-wave locators are combined. (For interpretation of the references to colour in this figure legend, the reader is referred to the web version of this article.)

smaller events, which are more likely to be observed on Mars. The teleseismic and regional events chosen are fairly deep (~30 km), which is suboptimal for surface-wave generation, but show that our location approach is applicable over a wide-range of (unfavorable) conditions.

We access the seismic waveforms and metadata for the three events from the SZGRF datacenter (www.szgrf.bgr.de) of the Federal Institute for Geosciences and Natural Resources (BGR), and downsample the waveforms to 10 sps corresponding to the sampling rate of waveforms returned from InSight. The following data processing is done within a GUI tool (marslocgui) based on SeisComp3 (www.seiscomp3.org) developed by the Swiss Federal Institute of Technology (ETH) Zurich and Gempa GmbH, in which the single-station approaches as proposed in this paper have been implemented. We band-pass filter the records with a second-order Butterworth filter with corner frequencies adapted to the frequency content of the respective event (Table 1).

For the location based on multi-orbit Rayleigh waves (Section 2.1), we pick the peak energy from *R1*, *R2*, and *R3* from the band-pass filtered (140–240 s) waveform envelopes in $N_B = 9$ frequency bands (Figs. 2b and 3b). For the small local event, we cannot identify *R1*, *R2* and *R3* arrivals and thus derive the location from body-wave phase-arrivals only.

For the location based on body- and surface wave arrivals (Section 2.2), we manually pick the phases along with their uncertainties from the waveforms inside the GUI (Table 1). We investigate two cases: in the first case, we assume that only *P* and *S* phases are picked, corresponding to the case of minimum information, and we use predicted secondary phase arrivals, such as of *pP* or *SP*, to verify the resulting distance estimate by matching them with clearly visible arrivals in the waveforms. In the second case, we examine how distance estimates change if additional phase arrivals and uncertainty ranges are picked, including depth and *R1* phases. We also explore how sensitive solutions are to incorrectly picked and mislabeled phases.

Unlike for the case of the Rayleigh locator (Section 2.1), locating seismic signals from body-wave phases requires theoretical travel times and uncertainties derived from available velocity models. Here, we use the *TauP Toolkit* 2.3 (Crotwell et al., 1999) to predict body-phase arrivals for various spherically symmetric 1-D velocity models from Earth. Furthermore, we adapt the *minor-based code* of Nolet (2008) to calculate fundamental-mode Rayleigh-wave group velocities and hence theoretical *R1* arrivals in various frequency bands (10–300 s).

To get a reasonable distribution of phase arrivals, we use eight standard Earth models that are distributed within the *TauP Toolkit*

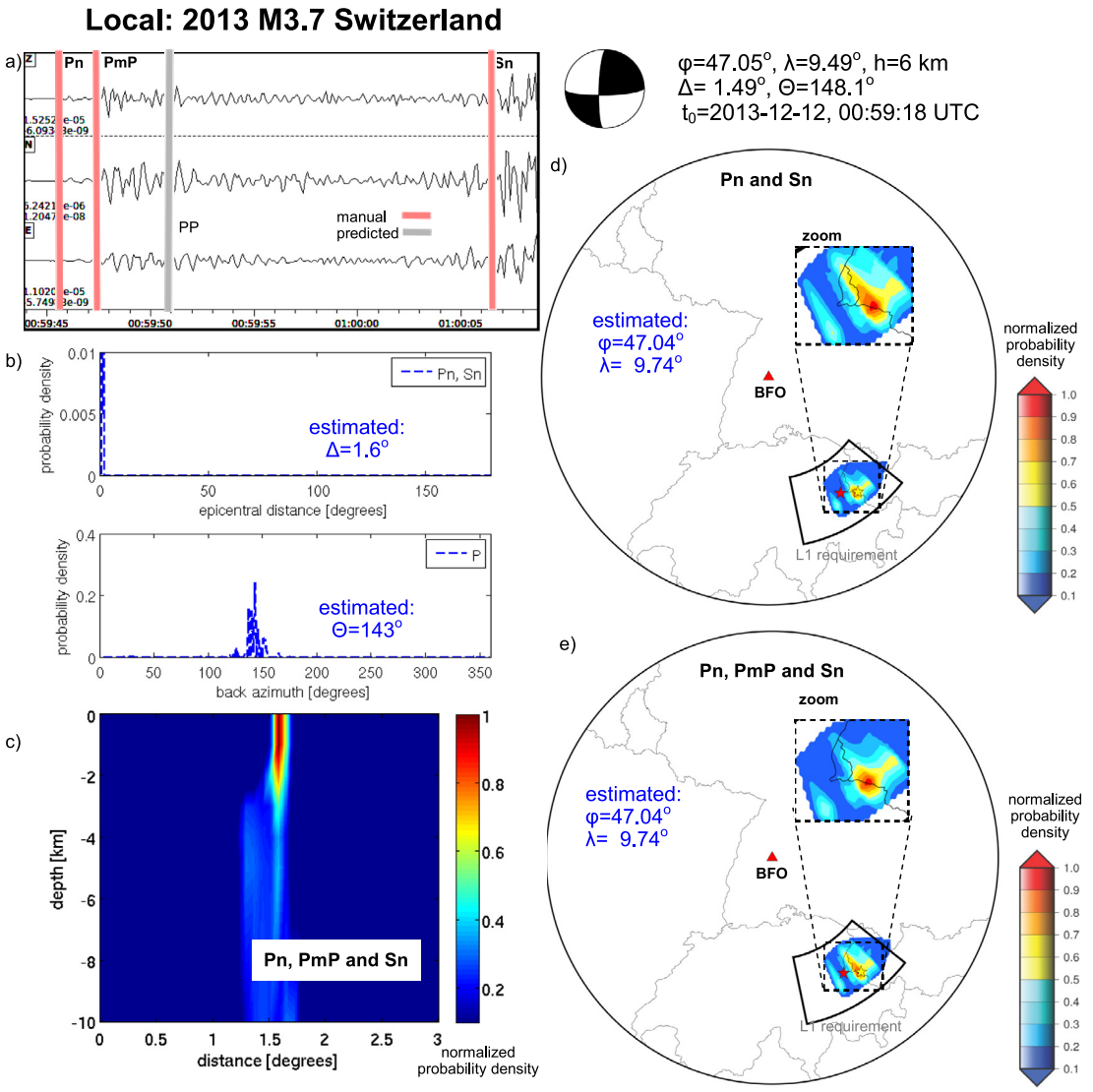


**Fig. 4.** Building a single-station probabilistic location for a small M3.7 earthquake at ~1.5° (local) distance from station BFO. See caption of Fig. 2 for explanation. *R1*, *R2*, and *R3* cannot be identified because of the small epicentral distance and small magnitude. The location estimates are derived from the body-phase picks of *Pn* and *Sn*, as well as the polarization of the *P*-wavetrain. Including the depth phase *PmP* allows resolving the event depth at <5 km (see c), and reduces location uncertainties (see d and e).

*2.3* (Crotwell et al., 1999). These are iasp91 (Kennett and Engdahl, 1991), PREM (Dziewonski and Anderson, 1984), ak135 (Kennett et al., 1995), jb (Jeffreys and Bullen, 1940), 1066a/b (Gilbert and Dziewonski, 1975), pwdk (Weber and Davis, 1990), and sp6 (Morelli and Dziewonski, 1993). Using a suite of models rather than a single model makes this test more similar to the Mars setting, in which the interior structure is largely unknown and models are poorly constrained.

The time window lengths for the back azimuth determination from the polarization of body- and surface waves vary from 5 s for the local event to 9 min for the teleseism (Table 1). Note, that the length of the selected time window is not critical for the results of our approach, but the time window should be chosen to encompass mostly *P*-wave energy.

### 3.2. Mars

For demonstration on Mars, we assume our reference station to be located at the target landing- site of the InSight lander in *Elysium Planitia* (φ = 4.5°, λ = 136.0°). To compute synthetic Martian seismograms, we use the axisymmetric spectral element method AxiSEM by Nissen-Meyer et al. (2014) and the Instaseis software by van Driel et al. (2015). These simulations are based on full numerical solutions of the visco-elastic wave equation and include the effects of attenuation, and are accurate down to 1 s period for body waves and 3 s for surface waves. We adapt a simple one-dimensional Martian velocity model as described in our companion paper (Khan et al., 2016), that was constructed using an average Martian mantle composition and model areotherm using thermodynamic principles, mineral physics data, and visco-elastic modeling. Depth profiles of *P*- and *S*-wave speeds, density $\rho$, and attenuation ($Q_\mu$) for crust, mantle and core are shown in Fig. 5. The sharp velocity increase at ~1100 km is caused by the mineral phase transition olivine->wadsleyite (more details are given in Khan et al. (2016)). The waveform simulations show strong reverberations caused by trapped energy in the crust that is produced by our simple crustal model.

Unlike on Earth, there is no microseismic noise on Mars as there are no oceans. The current power-spectral-density (PSD) model of the InSight noise working group (Murdoch et al., 2015a,b), which includes ambient and instrumental noise sources for both vertical and horizontal components, and day and night time (Fig. 6), is used to create realistic time-domain noise that is added to the simulated traces, assuming random phases with uniform distribution. Here

**Table 1**
Background information on the 3 earthquakes analysed in this study, as well as on the algorithms used. For the phase arrival algorithm, the identified body and surface phases, their actual pick times and uncertainties are shown; for the body-phase polarization, the optimal bandpass (BP) and time windows are indicated. The final location error combining solutions from all algorithms is given in terms of epicentral distance Δ and back azimuth Θ relative to station BFO, and absolute location loc. InSight L1 requirements which stipulate determining epicentral distances and back azimuths to accuracies of ±25% respective ±20° (Banerdt et al., 2013) are fulfilled.

| **Event**<br>moment magnitude<br>origin time<br>latitude/longitude/<br>depth<br>distance<br>back azimuth | **Algorithms** | **Errors**<br>epicentral<br>distance<br>back azimuth<br>absolute location |
|---|---|---|
| **Teleseismic**<br>M5.9 Peru<br>2015-06-29<br>09:09:21 UTC<br>-16.09°/-74.51°/<br>38 km<br>Δ = 97.3°<br>Θ = 254° | **Distance:**<br>- multi-orbit Rayleigh-phase arrivals (section 2.1)<br>- body-wave phase arrivals (section 2.2)<br>*P*: 09:22:43.1 ± 2.0 s<br>*S*: 09:33:58.0 ± 5.0 s<br>**Back azimuth:**<br>- Rayleigh wave (section 2.3)<br>- P-wave (section 2.4)<br>BP: 20–200 s,∼9 min | $\Delta_{error}$ = 0.2° (0.2%)<br>$\Theta_{error}$ = 1°<br>$loc_{error}$ = 0.99° |
| **Regional**<br>M5.6 Egypt<br>2015-06-27<br>15:34:03 UTC<br>28.83°/34.62°/<br>28 km<br>Δ = 28.1°<br>Θ = 124.4° | **Distance:**<br>- multi-orbit Rayleigh-phase arrivals (section 2.1)<br>- body- and surface-wave phase arrivals (section 2.2)<br>*P*: 15:39:54.1 ± 1.5 s<br>*S*: 15:44:37.2 ± 3.0 s,<br>*R1@120–180s:*<br>15:47:56.0 ± 30 s<br>**Back azimuth:**<br>- Rayleigh wave (section 2.3)<br>- P-wave (section 2.4)<br>BP: 10–50 s, ∼35 s | $\Delta_{error}$ = 1.0° (3.5%)<br>$\Theta_{error}$ = 0.4°<br>$loc_{error}$ = 1.0° |
| **Local**<br>M3.7<br>Switzerland<br>2013-12-12<br>00:59:18 UTC<br>47.05 °/9.49°/<br>6 km<br>Δ = 1.49°<br>Θ = 148.1° | **Distance:**<br>- body -wave phase arrivals (section 2.1)<br>*Pn*: 00:59:45.6 ± 0.25 s<br>*Sn*: 01:00:06.7 ± 0.65 s<br>*PmP*:00:59:47.5 ± 1.0 s<br>**Back azimuth:**<br>- P-waves (section 2.4)<br>BP: 1–2 s,∼5 s | $\Delta_{error}$ = 0.° (<0.1%)<br>$\Theta_{error}$ = 5.1°<br>$loc_{error}$ = 0.2° |

Source parameters obtained from www.globalcmt.org and www.seismo.ethz.ch.

we conservatively use the higher day-time noise. For comparison, at frequencies higher than 0.035 Hz (∼30 s), the noise at BFO, a high-quality Earth station relatively far from the oceans, is still significantly higher than what is expected on Mars, though at lower frequencies, this is reversed.

We model three events on Mars: teleseismic M5.0 at $\Delta \approx 97°$, regional M4.8 at $\Delta \approx 28°$, and local M3.4 at $\Delta \approx 8°$ (Figs. 7–9). Source locations and focal mechanisms of the simulated events agree with the corresponding example earthquakes in Section 3.1. In the case of the local event, however, we increase the distance and depth to 8.0° and 52 km, respectively, because our simple homogeneous crustal model (Fig. 5) produces unrealistically smooth waveforms for shallow events at close distances. We reduce the magnitudes of the simulated marsquakes to ∼85% of the corresponding earthquake to account for the more favorable noise conditions and expected lower seismicity on Mars (Table 2).

As for Earth we compute theoretical travel-time tables for various body-phases using the *TauP Toolkit* (Crotwell et al., 1999). On Mars, however, we need to use a wider range of models, since the interior structure of Mars is poorly constrained. As a proof-of-concept, we employ in this study a suite of 80 plausible Mars models (Fig. 5), obtained using methods described in Khan and Connolly (2008) and the parameterization of Khan et al. (2016). The reference model chosen to compute synthetic waveforms for Mars (colored lines in Fig. 5) is an extreme model with respect to the distribution of the model suite used to compute travel times, again to show that our location approach works well also under adverse conditions.

## 4. Results

*P*- and *S*-wave arrivals of all six events show quite impulsive onsets, so that we can pick them manually from the three-component seismograms in Figs. 2a, 3a, and 4a for Earth, and in Figs. 7a, 8a, and 9a for Mars. For the regional and teleseismic events, we pick additionally the multi-orbit Rayleigh phase arrivals *R1-R2-R3* from the waveform envelopes in various frequency bands (Figs. 2b, and 3b for Earth, and 7b and 8b for Mars); no multi-orbit arrivals are visible above background noise for the two small local events on Earth and Mars.

Using these pick times and their uncertainties (Tables 1 and 2), as well as the polarization of the respective *P*- and *R1* phases, we determine the probability density functions (PDFs) for epicentral distance and back azimuth relative to the recording station (Figs. 2c, 3c, 4b for Earth, and 7c, 8c, and 9b for Mars), as well absolute event locations (Figs. 2d, 3d, 4d for Earth, and Figs. 7d, 8d, 9d for Mars).

For the three example earthquakes, we determine absolute event locations to within 1.0° (∼111 km; ⩽3.5% relative distance error), for the three simulated marsquakes to within 0.6° (∼35 km; <5% relative distance error) relative to the given hypocenters. All locations are within the target uncertainty ranges set by the L1 requirements of the InSight mission (see thick lines in Figs. 2d–4d, and Figs. 7d–9d), which stipulate determining epicentral distances and back azimuths to accuracies of ±25% and ±20°, respectively (L1-SCI-51; Banerdt et al., 2013). It should be noted though that our synthetic marsquake waveforms were computed using a radial model, neglecting the complexities of the three-dimensional structure, in particular in the crust and upper mantle. We expect that three-dimensional effects will add larger uncertainties to the estimated event locations (see Discussion, Section 5).

The combination of multiple location approaches allows us to exploit the information contained in both body- and surface-waves. This helps to remove weaknesses of single methods and to obtain a more robust estimate of distance and back azimuth compared to the results obtained from each algorithm independently. For the M5.6 Egypt earthquake, for example, we cannot easily identify the *R2* arrival because of high noise amplitudes that result in an erroneous peak designation as most probable arrival (Fig. 3b). But since most of the solution candidates (Fig. 3c, black line) are inconsistent with the body-phase picks, they disappear in the combined solution (Fig. 3c, red line).

Aside from epicentral distance Δ, phase arrival times also depend on source depth *h*. Identified and picked depth phases, such as *PmP* or *pP* (see Section 2), are used in our body- and surface-wave phase arrival approach for distance estimation (Section 2.2) like any other phase. However, since these phases are strongly depth-dependent, we can apply equation (3.2) to determine $p_{body-surface}(\Delta, h)$ rather than the marginal $p_{body-surface}(\Delta)$ in Eq. (3.3), which we use in the other examples. This procedure is demonstrated here for the two local earth- and marsquakes, for which we pick *PmP* respective *pP* arrivals. Using these depth phases in combination with *Pn* and *Sn* (respective *P* and *S*) allows resolving the source depths of the two events as <5 km (Fig. 4c) and 45–75 km (Fig. 9c), respectively, which is in good agreement

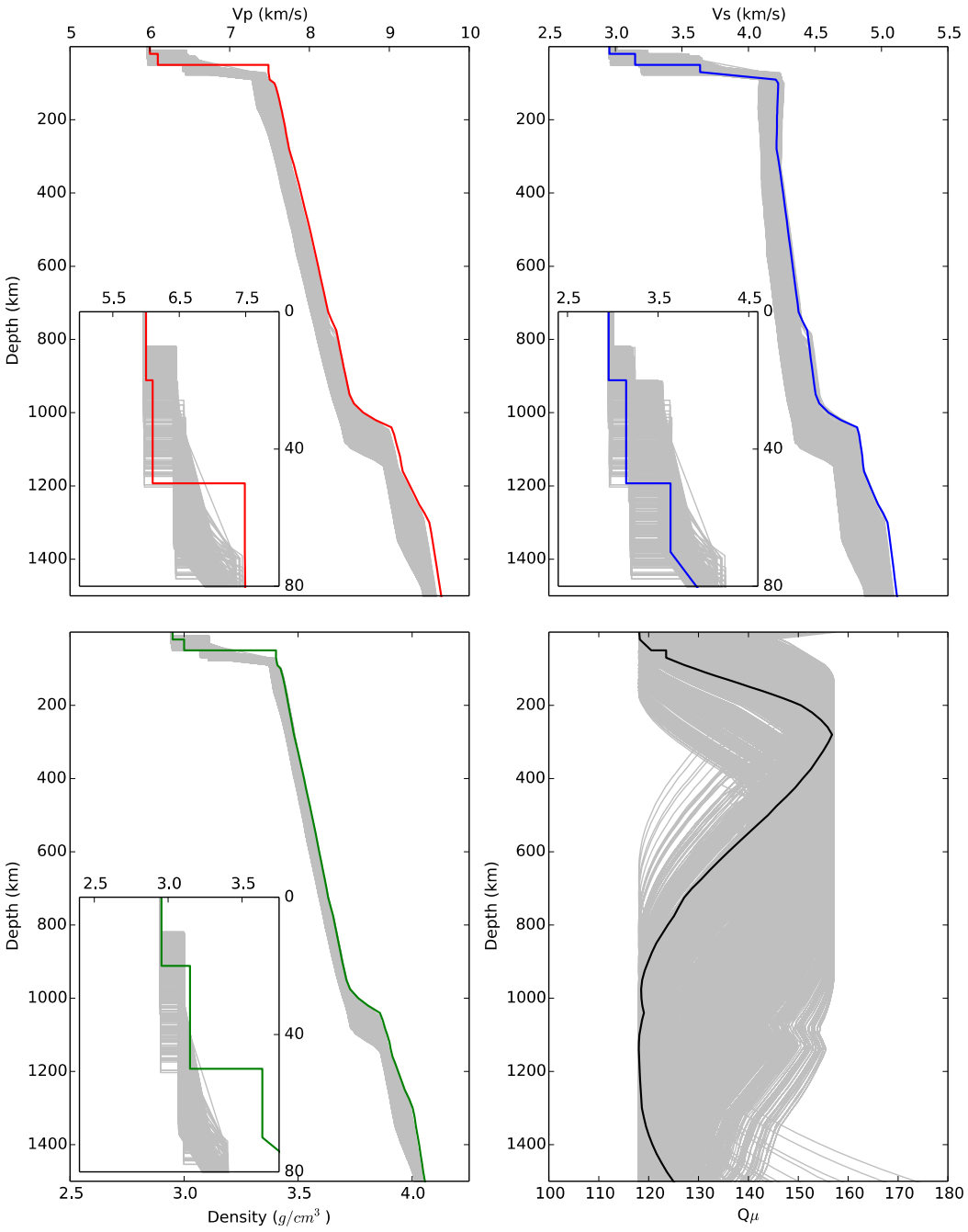


**Fig. 5.** One-dimensional *P*- and *S*-wave velocity $v_p$ and $v_s$ (top) and density and attenuation models (Q, bottom) for Mars described in our companion paper Khan et al. (2016). Thick colored lines show models used to generate Mars synthetic waveforms; gray lines show models used to locate quakes (only $v_p$ and $v_s$ are relevant).

with the given depths (Table 1). Using these depth phases in addition to other arrivals also helps reducing the uncertainties in our distance estimates (Figs. 4e and 9e).

With the estimated epicentral distances and available velocity models, we are able to predict the arrivals of secondary phases, such as *pP* or *SS*, and match those in the recorded seismograms. This is illustrated for various phases in the seismograms in Figs. 2a–4a and 7a–9a (gray bars). A good agreement between these predicted arrivals and observed changes in amplitudes and/or frequency content of the recorded waveforms indicates that a given distance estimate and assigned phase label is likely appropriate; otherwise we need to review our picks, phase labels, and location results. This iterative procedure of phase picking, forward modeling of additional phase arrivals, and comparison with the recorded waveforms needs to be repeated until all strong arrivals in the seismogram are explained. In our companion paper, Khan et al. (2016), this procedure is adapted for simultaneous inversion for structure.

To test the robustness of our approach, in the following, we analyse the sensitivity of our results to various possible shortcomings in the analysis, such as the number of phase picks, incorrect pick times, as well as mislabeled phases. We run these tests for three events from the original event suite.

### 4.1. Teleseismic M5.9 Peru

In this event we have very clear *R1-R2-R3* arrivals (Fig. 2b). We investigate two scenarios. In the first case (Fig. 10a, left), in addi-

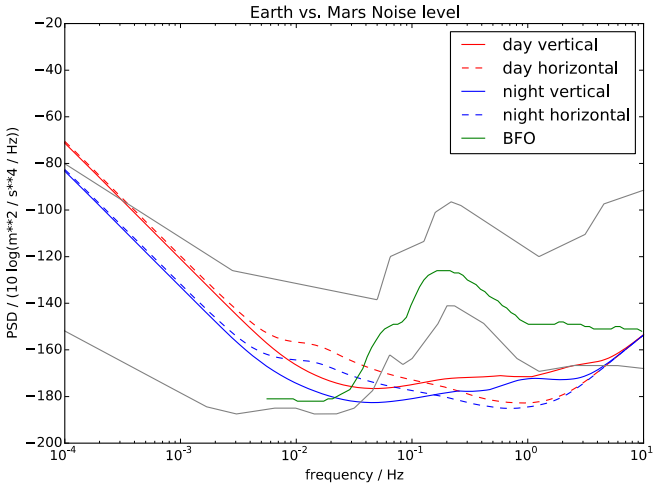


**Fig. 6.** Comparison of noise at Earth station BFO with noise models by Peterson (1993; gray lines) for Earth and by Murdoch et al., 2015a,b for Mars.

tion to *P* and *S*, we pick and correctly label *PP*. We show that we obtain a narrower peak in the distance PDF compared to the case when only *P* and *S* phases are used (Fig. 10b, left).

In the second scenario we correctly pick the *P* phase, but we mislabel the *SP* phase as *S*, denoted as $S^*$ (Fig. 10a, right). The locator tells us immediately that the time window between *P* and $S^*$ is too large for a direct arrival, so instead we label the second phase as *Sdiff*. We observe that the two distance PDFs from the picks (Fig. 10b, left) and *R1–R2–R3* (Fig. 10b, middle) do not overlap and no consistent solution is obtained, once we combine both solutions by multiplication (Fig. 10b, right), a strong indication that our picks are incorrect or mislabeled. In addition, with the distance estimated with the $S^*$ pick (120°, Fig. 10b left), the predicted *PP* arrival (shaded area in Fig. 10a, right) will no longer line up with the clear phase seen in Fig. 10a, left. This example demonstrates how phase identifications can be iteratively improved in case of erroneous phase labeling or picking.

### 4.2. Regional M5.6 Egypt

In this event we have no clear *R1–R2–R3* arrivals and thus multiple solutions in the resulting distance PDF (Figs. 3b and 3c). We investigate three scenarios: (1) in addition to *P* and *S* (Fig. 10c, left) we pick and correctly label *R1* measured between 120 and 180 s and denoted as *R1@120–180s*, (2) we correctly pick *P*, but pick the *S* phase 20 s too late (here denoted as $S^*$; Figure 10c, right); (3) we pick the same $S^*$ phase as in (2), but assign to this pick a

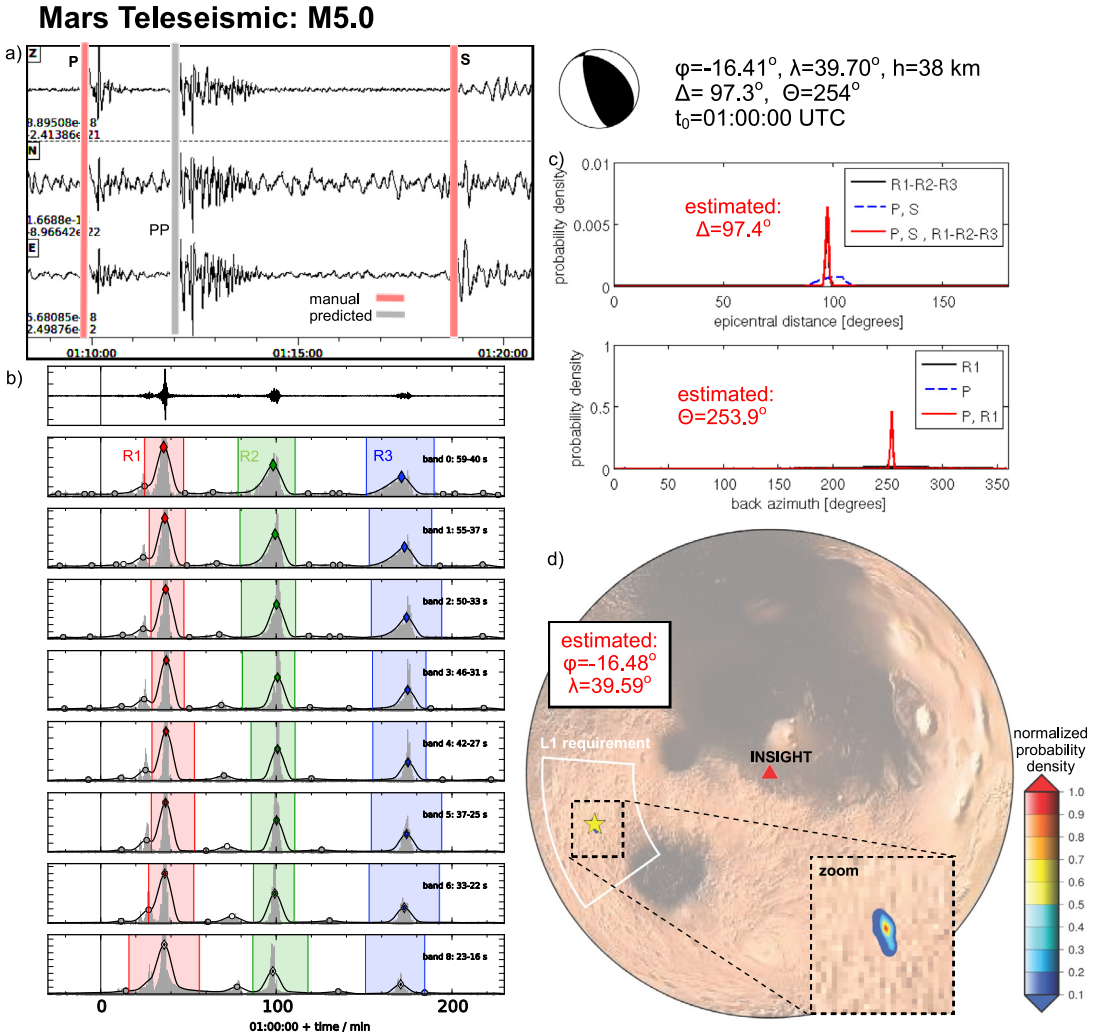


**Fig. 7.** Building a single-station probabilistic location for a moderate-sized M5.0 synthetic marsquake at ~97° (teleseismic) distance from the InSight landing site. Trapped crustal reflections produce strong reverberations and long wavetrains, such as of the *pP* phase. See caption of Fig. 2 for explanation.

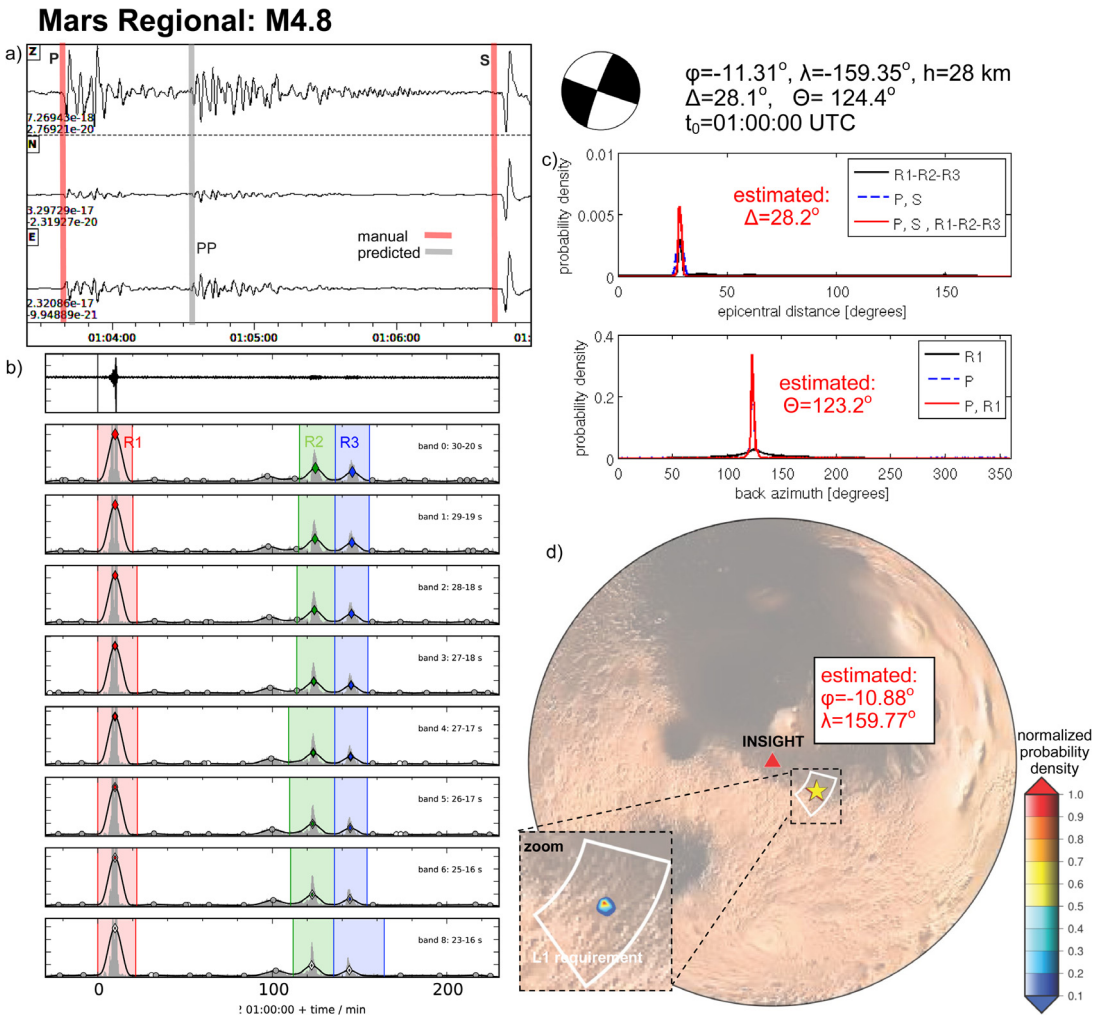


**Fig. 8.** Building a single-station probabilistic location for a moderate-sized M4.8 synthetic marsquake at ~28° (regional) distance from the InSight landing site. See caption of Fig. 2 for explanation.

large uncertainty of 25 s, which actually includes also the correct arrival *S*. In the first case, when we supplement *P* and *S* arrivals by *R1@120-180s*, we obtain a more peaked distance PDF compared to the case when using only *P* and *S* (Fig. 10d, left). When combined with the results from *R1–R2–R3* (Fig. 10d, middle), it becomes clear that distances beyond 40° are not expected (as predicted from multiple solutions from *R1–R2–R3*). When using *R1* in addition to the two body-wave phase picks, we obtain a better defined, that is higher peaked distance result compared to the case of minimum information (Fig. 10d, right).

In the second scenario, in which we pick the *S* phase arrival 20 s too late (Fig. 10c, right), the event is estimated to be located at larger distance (>29°, Fig. 10d, left). As the results from *R1–R2–R3* do not help in this case, and the probability in the combined distance PDF for the correct distance at 28.1° is low (Fig. 10d, right). However, the probability increases significantly in the third scenario, in which we assign a larger uncertainty to *S**. Unlike in the previous example of the teleseismic Peru earthquake, there are no clear secondary picks in this event that we can use to verify predicted secondary phase arrivals.

### *4.3. Local M3.4 Mars*

There are two complications with this event: first, we have no results from the *R1–R2–R3* approach, and, second, *P* and *pP* arrivals are very weak (Fig. 10e, left). We investigate here two scenarios: (1) in addition to *P* and *S* we pick and correctly label *pP* (Fig. 10e, left), and (2) we correctly label the *S* phase, but mislabel the *P^20S* arrival as *P* (here denoted *P**; Fig. 10c, right). In the first case, we see that the correct distance at 8° is not well-covered by the PDF (Fig. 10f, left). The problem here is, that our reference model for the waveform simulations is extreme compared to the model suite used for location (cfr. Fig. 5); under these conditions, adding more phases generates multiple solutions for the distance recovery, contrary to what we observe on the Earth, where the model is better constrained.

In the second scenario, in which we mislabel the *P^20S* arrival as *P*, the event is estimated as being located at closer distance (Fig. 10f, left). Detecting this error is challenging in this case, since the *R1–R2–R3* approach cannot be used for a small local quake. This event highlights the need for careful review of all picks with synthetics and updated models to spot errors.

## 5. Discussion

The amplitudes and travel-times of Rayleigh waves are controlled primarily by event magnitude and distance with respect to the recording station, but are also sensitive to azimuth, focal depth, mechanism, rupture directivity, and geologic structure

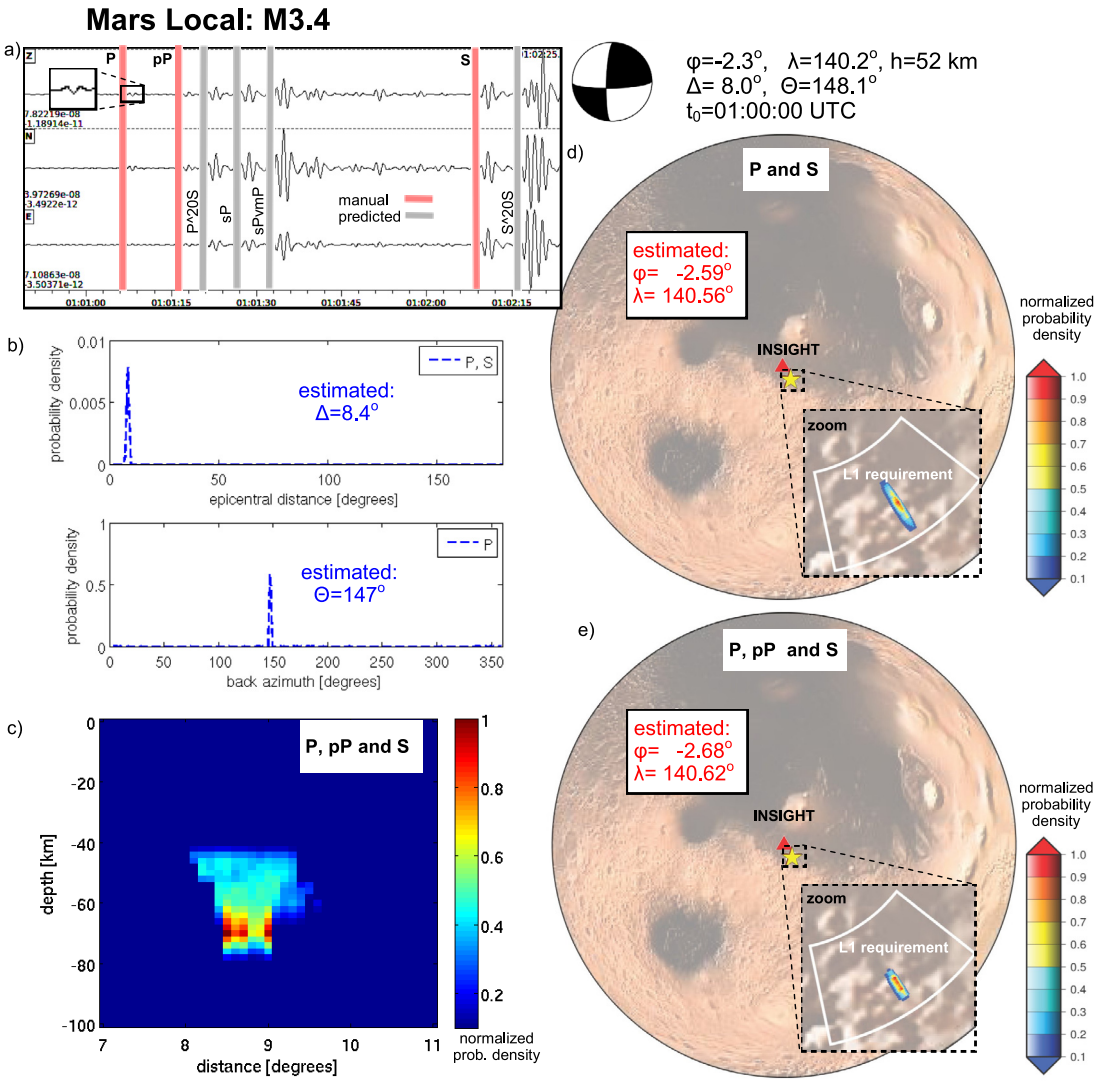


**Fig. 9.** Building a single-station probabilistic location for a moderate-sized M3.4 synthetic marsquake at 8° (local to regional) distance from the InSight landing site. See caption of Fig. 2 for explanation. Phase arrivals between *P* and *S* are caused by energy that enters the crust as *S*-wave and then is trapped above the Moho. The most prominent phase is *SPvmP*, where *vm* denotes an upper side Moho reflection (see Electronic Supplements for wave-animation). Including the depth phase *pP* allows constraining the event depth at ~45–75 km in c) and reduces absolute location uncertainties in e).

along the travel path. The time window between the full-orbit *R3* phase arrivals on Mars is 3 h, compared to 4½ hours on Earth, which is about twice the size in circumference of Mars. Due to the shorter propagation distances, Rayleigh waves on Mars are expected to be less attenuated and *R3* phases should still be detectable at teleseismic distances for magnitude ~M5 quakes, compared to ~M6 on Earth (Panning et al., 2015). Moreover, Larmat et al. (2008) predict that surface-wave dispersion on Mars is likely smaller than on Earth and Rayleigh waves are hence more impulsive and easier to observe. Nevertheless, there are a number of issues potentially affecting the location accuracy derived from Rayleigh wave observations.

First, the Rayleigh wave approaches as outlined in Sections 2.1 and 2.3 assume an idealized spherically symmetric planet. The strong ellipticity of Mars, which is ~1.76 larger than on Earth (http://nssdc.gsfc.nasa.gov/planetary/factsheet/marsfact.html), will change Rayleigh-wave travel-times and thus distance and origin time estimates. Secondly, geometrical effects caused by the extreme variability in surface topography on Mars ranging from −8 km in the *Hellas impact basin* to 20 km on *Olympus Mons* is expected to increase travel-times in basins and to decrease those with high elevations (Larmat et al., 2008).

Thirdly, lateral phase velocity variations, which on Earth can be as large as 10% and may be even larger on Mars, can lead to significant deviations of the Rayleigh wave paths from the great circle and may cause anomalies of surface wave amplitudes and polarization (e.g., Romanowicz, 2002). These anomalies can often be associated with focusing and defocusing effects related to caustics formed by the intersection of surface wave paths at large epicentral distances, that can particularly affect the multi-orbit phases *R2*, *R3*, etc. (Bukchin et al., 2006). Schwartz and Thorne (1987), however, find that for most source-receiver geometries on Earth, the off great-circle travel-time differences for second and third orbits are small (<10 s), which suggests that the effect on estimates of Δ and $t_0$ should be minor.

Lateral structural variations in the Martian crust are likely much stronger than on Earth (Larmat et al., 2008) due to the crustal dichotomy between the Southern and Northern hemispheres (e.g., Zhong and Zuber, 2001): the crust in the Northern lowlands with an estimated average thickness of ~30 km, is only half as

**Table 2**
Background information on the 3 synthetic marsquakes analysed in this study, as well as on the algorithms used. Follows Table 1.

| **Event**<br>moment magnitude<br>origin time<br>latitude/longitude/<br>depth<br>distance<br>back azimuth<br>strike/dip/rake | **Algorithms** | **Errors**<br>epicentral<br>distance<br>back azimuth<br>absolute location |
|---|---|---|
| **Teleseismic**<br>M5.0<br>01:00:00 UTC<br>-16.41°/39.70 °/<br>38 km<br>$\Delta$ = 97.3°<br>$\Theta$ = 254 °<br>313°/29°/63° | **Distance:**<br>-multi-orbit Rayleigh-phase arrivals (section 2.1)<br>- body-wave phase arrivals (section 2.2)<br>*P*: 01:09:51.3 ± 5 s<br>*S*: 01:18:45.0 ± 10 s<br>**Back azimuth:**<br>- Rayleigh wave (section 2.3)<br>- P-wave (section 2.4)<br>BP: 1–10 s, ∼1 min | $\Delta_{error}$ = 0.1° (0.1%)<br>$\Theta_{error}$ = 0.1°<br>$loc_{error}$ = 0.1° |
| **Regional**<br>M4.8<br>01:00:00 UTC<br>-11.31°/159.35° /<br>28 km<br>$\Delta$ = 28.1°<br>$\Theta$ = 124.4°<br>200 °/82 °/2° | **Distance:**<br>- multi-orbit Rayleigh-phase arrivals (section 2.1)<br>- body-wave phase arrivals (section 2.2)<br>*P*: 01:03:40.0 ± 5.0 s<br>*S*: 01:06:40.0 ± 10.0 s<br>**Back azimuth:**<br>- Rayleigh wave (section 2.3)<br>- P-wave (section 2.4)<br>BP: 1–10 s, ∼30 s | $\Delta_{error}$ = 0.1° (0.4%)<br>$\Theta_{error}$ = 1.2°<br>$loc_{error}$ < 0.6 ° |
| **Local**<br>M3.4<br>01:00:00 UTC<br>-2.3°/140.2°/<br>52 km<br>$\Delta$ = 8.0°<br>$\Theta$ = 148.1°<br>182°/77°/15° | **Distance:**<br>- body -wave phase arrivals (section 2.1)<br>*P*: 01:01:06.7 ± 0.4 s<br>*S*: 01:02:09.0 ± 2.0 s<br>*pP*:01:01:16.5 ± 0.5 s<br>**Back azimuth:**<br>- P-wave (section 2.4)<br>BP: 1–20 s, ∼25 s | $\Delta_{error}$ = 0.4° (5%)<br>$\Theta_{error}$ = 1°<br>$loc_{error}$ = 0.5° |

thick as in the Southern highlands. Surface waves travelling across the thin Northern hemisphere are characterized by earlier arrivals compared to those travelling across the Southern hemisphere (Larmat et al., 2008).

Though ellipticity, topography, and lateral phase velocity variations are expected to change surface wave propagation on Mars, these effects can be modeled in advance to determine empirical correction factors that can be applied to the later recorded seismic events (Lognonné and Johnson, 2007) once preliminary azimuths and distances are determined. Our preliminary back-of-the-envelope calculations suggest that the Martian ellipticity may cause errors in $\Delta$ and $t_0$ of up to ∼0.5° (∼30 km) and ∼10 s, respectively, while the crustal dichotomy with errors of ∼7° (∼420 km) and ∼70 s is expected to have a much larger impact. A more detailed study of these effects is under way and will be discussed in forthcoming publications.

Not only distance, but also back azimuth estimates are affected by the divergence of Earth and Mars from the idealized planet model in which perfect elliptical polarization is predicted. The accuracy of the back azimuth measurement typically decreases with the amplitude of the signal. Chael (1997) find that back azimuth errors on Earth are typically ±15° for Ms > 4 and $\Delta \leqslant 30°$; the sensitivity decreases gradually to ∼ Ms5 at the furthest ranges. Using a location approach similar to the multi-orbit and back azimuth Rayleigh approaches we have been using here, Panning et al. (2015) find that for terrestrial seismic data, most events (M > 6) are located within an epicentral distance of 1° and an origin time of 30 s; back azimuth errors are typically within 10°.

According to Selby (2001), back azimuth errors using *R1* polarization are mainly caused by (1) interference of Rayleigh waves with Love waves or with scattered Rayleigh or Love waves; (2) off great-circle path propagation of Rayleigh waves; (3) deflection of the plane of the polarization ellipse from the plane of propagation due to azimuthal anisotropy; (4) much higher noise at periods >50 s (on Earth) on the horizontal components than on the vertical component, mainly caused by atmospheric pressure and/or wind. Peak amplitudes of *R1* Rayleigh waves from shallow earthquakes, however, are typically observed at ∼20 s period, so the last problem can be largely avoided (at least on Earth) by choosing appropriate frequency bands for the back azimuth measurements (Selby, 2001). The approach is likely more feasible on Mars where the lack of microseisms may lead to low noise in this frequency range. The Rayleigh wave method described in this paper could in principal be extended to Love waves, which cause pure transverse horizontal motion along the planet surface. However, employing Love waves for seismic event location requires usage of horizontal waveforms, which are typically much noisier than those on the vertical component.

Walck and Chael (1991) find that quite accurate back azimuth estimates can be obtained from *P*-wave polarization analyses of regional earthquakes with >75% of the records yielding errors of less than 20°. The accuracy of the back azimuth estimates, however, does vary from station to station. In general, the choice of frequency band plays the most important role, while the length of the signal window is less critical, which is consistent with our preliminary observations. Using the polarization of seismic body waves for back azimuth measurements requires a significant level of coherence among the three orthogonal components of ground motion. In strongly scattered environments, such as observed on the Moon (Nakamura, 1977), the lack of coherence prohibits polarization analyses and back azimuth estimates. Both the level of dissipation (*Q*) and scattering of seismic waves on Mars are not well known.

In this study, we assume that phase arrivals are uncertain in time due to noise and limited temporal resolution. In practice, correct phase identification, is often challenging, in particular for depth and core phases, such as *pP*, *sP*, *sS*, *PcP*, or *ScS*. One way to avoid phase mis-identification is to utilize generic phase labels, such as *P1* or *S1*, in order to identify *any* first *P* or *S* arrival (provided that corresponding travel-time tables exist). Alternatively, we may want to iteratively predict secondary phase arrivals (for a preliminary distance estimate from our approach) and compare these with observed waveform anomalies as discussed in Section 4 and also in our companion paper (Khan et al., 2016). This procedure can also encompass depth phases, and might in addition to pure arrival times involve waveforms, possibly with the horizontal components rotated in radial and transversal directions using the estimated back azimuth. Once a preliminary distance is estimated from our location approach, we can vary the source depth *h* to check for a good match with one or more depth phases (here *pP*) in the simulated and recorded waveforms. This is demonstrated in Fig. 11 using the example of the deep local marsquake.

We demonstrated in this paper a procedure to locate seismicity from body- and surface-wave arrivals. In general, the accuracy of estimated source locations is expected to increase with increasing numbers of picked phases (see Fig. 5 for example). The sensitivity of the InSight very-broadband (VBB) seismometer is expected to be comparable to that of the best terrestrial seismometers (Lognonné et al., 2012; Lognonné and Pike, 2015). External noise is anticipated to originate mainly from temperature, pressure, and wind fluctuations. Due to the absence of oceans, which is the major source of

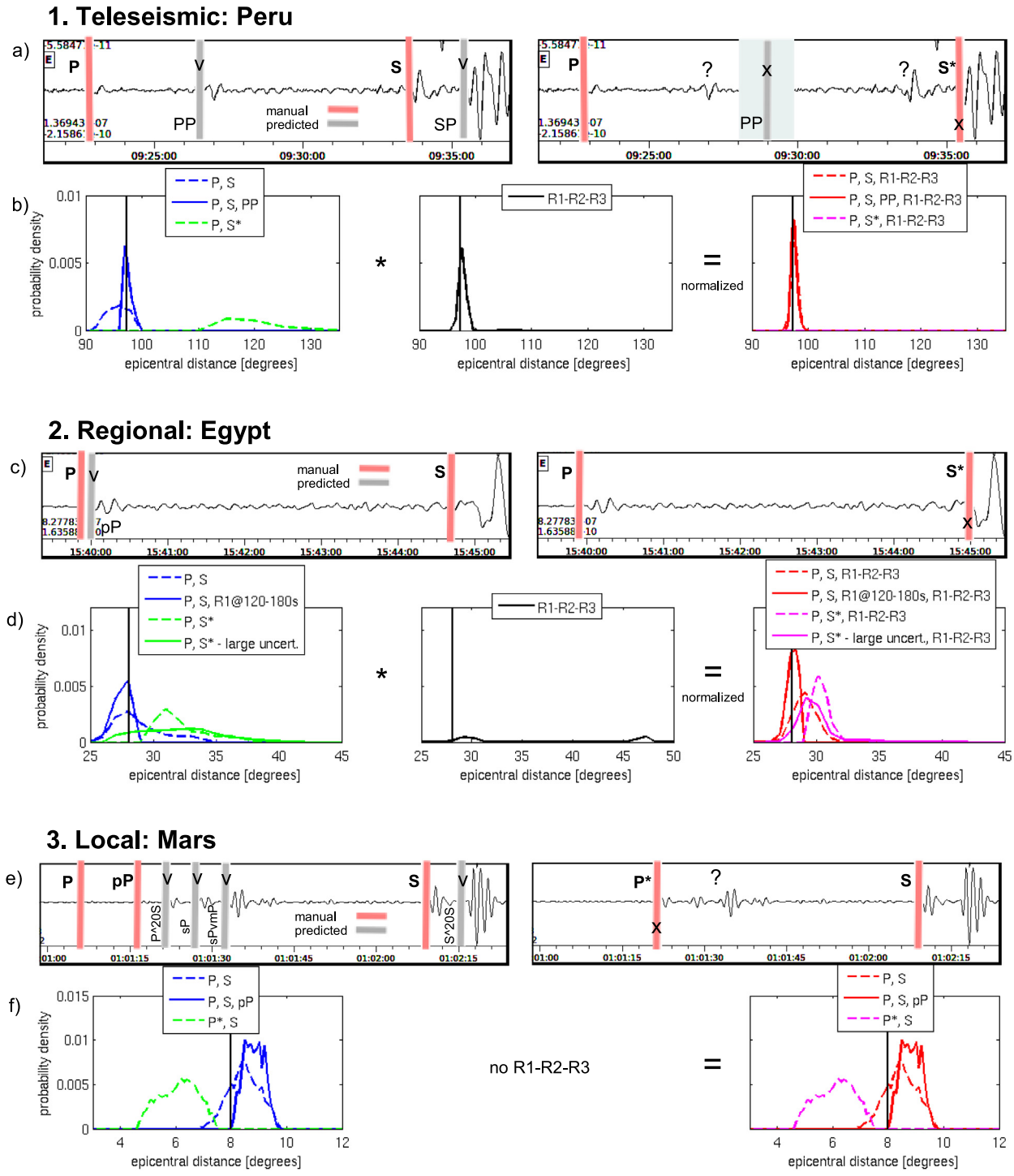


**Fig. 10.** Probability density functions for epicentral distances Δ of the (1) teleseismic M5.9 Peru earthquake at Δ = 97.3° (Fig. 2), (2) regional M5.6 Egypt earthquake at Δ = 28.1° (Fig. 3), and (3) local M3.4 marsquake at Δ = 8.0° (Fig. 9) using different pick scenarios to explore the sensitivity of solutions towards additional picks, mislabeled phases, and incorrect picks ("v" marks correct and "X" incorrect picks). See main text for details.

terrestrial noise between 1 and 30 s, seismic noise on Mars in this frequency band is expected to be generally low ($\sim 10^{-9}$ m/s$^2$ at 0.5 Hz; Banerdt et al., 2013). While diffusive scattering clearly dominates the seismic records from the Moon and often prohibits the separation of individual seismic phases (including *P* and *S*) and polarization analyses (Nakamura, 1977), Martian records are expected to be less challenging to interpret: first, strong scattering requires extreme low-volatile conditions (for very high *Q*), which are not expected on Mars; secondly, the effects of both dissipation and scattering should be less pronounced at the lower frequencies (<0.1 Hz) on the VBB sensor. It is expected that *P*- and *S*-waves from a quake of $10^{15}$ Nm ($\sim m_b = 4$) can be detected globally with signal-to-noise-ratios of >5 for a sensitivity of $10^{-9}$ m/s$^2$ (Banerdt et al., 2013).

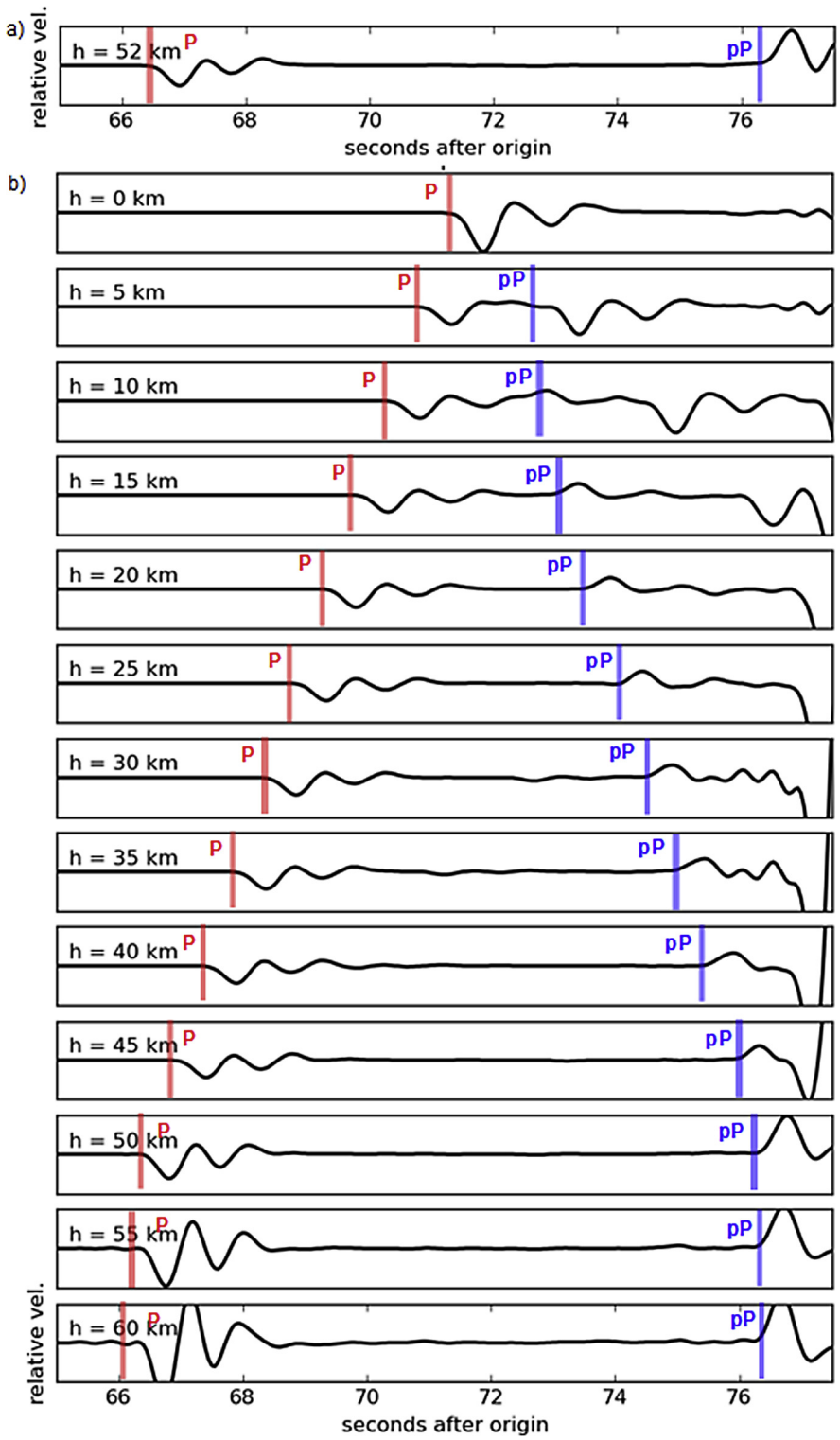


**Fig. 11.** Once the epicentral distance Δ is estimated, correctly identified and picked depth phase arrivals, such as *pP* or *sP*, help constraining event depth *h*. a) Initial portion of the vertical component velocity seismogram of the local M3.4 marsquake synthetic at Δ = 8° distance and *h* = 52 km depth shown in Fig. 9 with picked *P* and *pP* arrivals. b) Variations in source depth *h* of the same quake between 0 and 60 km and resulting *P* and *pP* arrivals.

## 6. Conclusions

In this paper, we propose and verify a new framework for locating seismic activity using three-component broadband data recorded on a single-station. Locating seismic energy using limited data is a major challenge due to difficulties in phase identification and large inherent pick and model uncertainties. We have developed a probabilistic framework for single-station location in which we combine multiple algorithms that use independent and complementary information in the seismic signals to estimate the probability density function of epicentral distance Δ and back azimuth Θ. First, multi-orbit Rayleigh arrivals $t_{R1}$, $t_{R2}$ and $t_{R3}$ are

picked in various frequency bands to estimate $p_{R1\ R2\ R3}(\Delta)$. Second, two or more body and surface phase arrivals (e.g. $t_P$, $t_S$, and $t_{R1@120s}$) and their uncertainties are picked and compared with theoretical arrivals predicted from a suite of velocity models, to produce $p_{body\text{-}surface}(\Delta)$. $p_{R1}(\Theta)$ and $p_P(\Theta)$ are estimated from the polarization of the *R1*- and body-waves, respectively. Estimates from the various methods are combined through the product of their PDFs, which usually results in a well-defined event location and uncertainty range.

We combine four methods: two methods for determining epicentral distance, and two methods for determining the back azimuth relative to the receiver. Other methodologies, such as cross-correlation techniques, can be added to the proposed framework in the future. We expect that these methods will additionally improve location estimates. Also likely marsquake locations, e.g. constrained by surface faults and other parameters (Knapmeyer et al., 2006), could be included as *prior* information. This approach appears particularly intriguing to assign source depth to events, where no depth phases can be identified.

While developed for the planned InSight NASA mission that will deploy a single seismic station on Mars in November 2018, our probabilistic approach is also relevant to locate quakes on Earth in regions with sparse instrumentation. As shown in this paper, the method shows good performance for local, regional and teleseismic events, as long as body phases and/or Rayleigh wavetrains are identifiable above the station noise. A joint location and inversion-scheme based on our location approach is discussed in our companion paper (Khan et al., 2016).

## Acknowledgements

We would like to thank Jan Becker from Gempa GmbH for integration of our proposed probabilistic framework for single-station location in the marslocgui tool. We would also like to thank Naomi Murdoch and David Mimoun for making their Martian noise model available prior to publication. This work was funded by joint SNF-ANR project 157133 'Seismology on Mars' and the SEFRI project 'MarsQuake Service - Preparatory Phase'. Additional support came from a grant from the Swiss National Supercomputing Centre (CSCS) under project IDs s528 and s682. We would like to thank an anonymous reviewer and editor Mark Jellinek for their comments. This is InSight contribution #12.

## Appendix A.

In the extended Rayleigh approach for distance estimation (Section 2.1), we consider all $i = 1\ldots N_i$ peak combinations in the waveform envelopes assuming that $t^{(i)}_{R1_b} > t^{(i)}_{R2_b} > t^{(i)}_{R3_b}$. The corresponding probability density functions $f(X^{(i)})$ are modeled as Gaussian distributions

$$f(X^{(i)}) = \frac{1}{\sigma_X^{(i)}\sqrt{2\pi}} e^{-0.5\left(\frac{X^{(i)}-\bar{X}^{(i)}}{\sigma_X^{(i)}}\right)^2}, \quad X^{(i)} = \{\Delta^{(i)}, t_0^{(i)}\} \tag{A1}$$

with mean $\bar{X}^{(i)}$ and standard deviation $\sigma_X^{(i)}$ given by

$$\bar{X}^{(i)} = \frac{\sum_{b=1}^{N_b} \tilde{w}_b^{(i)} X_b^{(i)}}{\sum_{b=1}^{N} \tilde{w}_b^{(i)}} \quad \text{and} \quad \sigma_X^{(i)} = \sqrt{\frac{\sum_{b=1}^{N_b} \tilde{w}_b^{(i)} (X_b^{(i)} - \bar{X}_b^{(i)})^2}{\sum_{b=1}^{N_b} \tilde{w}_b^{(i)}}} X_b^{(i)}$$
$$= \{\Delta_b^{(i)}, t_{0_b}^{(i)}\} \tag{A2}$$

and normalized weights

$$\tilde{w}_b^{(i)} = \frac{w_b^{(i)}}{\max_b(w_b^{(i)})}, \text{ where } w_b^{(i)} = \frac{\widehat{R1}_b^{(i)} + \widehat{R2}_b^{(i)} + \widehat{R3}_b^{(i)}}{3} \cdot \int_{U_b^{(i)}-\delta u}^{U_b^{(i)}+\delta u} g(u)du \tag{A3}$$

That is, each solution $i = 1\ldots N_i$ (assuming their consistent existence in multiple frequency bands) is weighted by the mean per-band normalized peak envelope amplitudes $\widehat{R1}_b^{(i)}$, $\widehat{R2}_b^{(i)}$ and $\widehat{R3}_b^{(i)}$ and the probability of

$$g(U) = \frac{1}{\sigma_U\sqrt{2\pi}} e^{-0.5\left(\frac{U-\bar{U}}{\sigma_U}\right)^2} \tag{A4}$$

at group velocity $U_b^{(i)} \pm \delta u$. Here we set $\bar{U} = 3.6$ km/s and $\sigma_U = 0.75$ - km/s for Earth, and $\bar{U} = 2.5$ km/s km/s and $\sigma_U = 0.75$ km/s for Mars, which is in good agreement with the dispersion curves observed for Earth (e.g. Panning et al., 2015) and estimated for Mars (Khan et al., 2016).

The final PDF $p_{R1\ R2\ R3}(X)$ with $X = \{\Delta, t_0\}$ is obtained from summing up the PDFs of all weighted solutions

$$p_{R1R2R3}(X) \propto \sum_{i=1}^{N_i} \tilde{w}_{all}^{(i)} \cdot f(X^{(i)}) \tag{A5}$$

where

$$\tilde{w}_{all}^{(i)} = \frac{w_{all}^{(i)}}{\max(w_{all}^{(i)})}, \quad w_{all}^{(i)} = \left(\sum_{b=1}^{N_b} \tilde{w}_b^{(i)}\right). \tag{A6}$$

## Data and resources

Earth station BFO is operated jointly by the Karlsruhe Institute of Technology and the Stuttgart University. The data from the broadband seismometer STS-2 are archived and disseminated by the SZGRF datacenter (www.szgrf.bgr.de) of the Federal Institute for Geosciences and Natural Resources (BGR). Source parameters were obtained from the Global Centroid-Moment-Tensor (CMT) catalogue (www.globalcmt.org; last accessed January 2016) and the Swiss Seismological Service event catalogue (www.seismo.ethz.ch). Synthetic seismograms for the three marsquakes were computed with the axisymmetric spectral element AxiSEM code (Nissen-Meyer et al., 2014). Maps were generated with Generic Mapping Tools (GMT; Wessel et al., 2013), using the MOLA (Mars Orbiter Laser Altimeter; Smith et al., 2001) dataset.

## Appendix B. Supplementary data

Supplementary data associated with this article can be found, in the online version, at http://dx.doi.org/10.1016/j.pepi.2016.11.003.

## References

Agius, M.R., Galea, P., 2011. A single-station automated earthquake location system at Wied Dalam Station, Malta. Seismol. Res. Lett. 82 (4), 545–559.
Anderson, D.L., Kovach, R.L., Latham, G., Press, F., Toksöz, M.N., Sutton, G., 1972. Seismic investigations: the viking mars lander. Icarus 16, 205–216.
Anderson, D.L., Miller, W.F., Latham, G.V., Nakamura, Y., Toksöz, M.N., Dainty, A.M., Duennebier, F.K., Lazarewicz, A.R., Kovach, R.L., Knight, T.C.D., 1977. Seismology on Mars. J. Geophys. Res. 82, 4524–4546.
Baker, G.E., Stevens, J.L., 2004. Back azimuth estimation reliability using surface wave polarization. Geophys. Res. Lett. 31, L09611. http://dx.doi.org/10.1029/2004GL019519.
Banerdt, W.B., Smrekar, S., Lognonné, P., Spohn, T., Asmar, S.W., Banfield, D., Boschi, L., Christensen, U., Dehant, V., Folkner, W., Giardini, D., Goetze, W., Golombek, M., Grott, M., Hudson, T., Johnson, C., Kargl, G., Kobayashi, N., Maki, J., Mimoun, D., Mocquet, A., Morgan, P., Panning, M., Pike, W.T., Tromp, J., van Zoest, T.,

Weber, R., Wieczorek, M.A., Garcia, R., Hurst, K., 2013. InSight: A Discovery Mission to Explore the Interior of Mars, in Lunar and Planetary Science Conference, Lunar and Planetary Inst. Technical Report, 44, p. 1915.
Böse, M., Heaton, T.H., Hauksson, E., 2012. Rapid estimation of earthquake source and ground-motion parameters for earthquake early warning using data from a single three-component broadband or strong-motion sensor. Bull. Seismol. Soc. Am. 102 (2), 738–750. http://dx.doi.org/10.1785/0120110152.
Bukchin, B.G., Yanovskaya, T.B., Montagner, J.-P., Mostinskiy, A.Z., Beucler, E., 2006. Surface wave focusing effects: numerical modeling and statistical observations. Phys. Earth Planet. Inter. 155 (3–4), 191.
Chael, E., 1997. An automated Rayleigh-wave detection algorithm. Bull. Seismol. Soc. Am. 87, 157–163.
Crotwell, H.P., Owens, T.J., Ritsema, J., 1999. The TauP Toolkit: flexible seismic travel-time and ray-path utilities. Seismol. Res. Lett. 70, 154–160.
Diehl, T., Kissling, E., Bormann, P., 2011. Tutorial for consistent phase picking at local to regional distances. In: Bormann, Peter (Ed.), New Manual of Seismological Observatory Practice (NMSOP-2). IASPEI, GFZ German Research Centre for Geosciences, Potsdam, p. 21. http://dx.doi.org/10.2312/GFZ.NMSOP-2_IS_11.4. Chapter: IS 11.4.
Dziewonski, A.M., Anderson, D.L., 1981. Preliminary reference Earth model. Phys. Earth Planet. Inter. 25, 297–356. http://dx.doi.org/10.1016/0031-9201(81)90046-7.
Dziewonski, A.M., Anderson, D.L., 1984. Structure, elastic and rheological properties and density of the Earth's interior, gravity and pressure. Geophysics of the Solid Earth, the Moon and the Planets. Zahlenwerte und Funktionen aus Naturwissenschaften und Technik, Gruppe V, Geophysik und Weltraumforschung. Springer, Berlin, pp. 84–96. ISBN 9783540122098.
Dziewonski, A.M., & Romanowicz, B., 2007. Overview of Volume I: Seismology and structure of the Earth, Treatise of Geophysics, 1.
Eisermann, A.S., Ziv, A., Wust-Bloch, G.H., 2015. Real-time back azimuth for earthquake early warning. Bull. Seismol. Soc. Am. 105 (4). http://dx.doi.org/10.1785/0120140298.
Frohlich, C., Pulliam, J., 1999. Single-station location of seismic events: a review, and a plea for more research. Phys. Earth Planet. Int. 113, 277–291.
Gagnepain-Beyneix, J., Lognonné, P., Chenet, H., Spohn, T., 2006. Seismic models of the Moon and their constraints on the mantle temperature and mineralogy. Phys. Earth Planet. Int. 159, 140–166. http://dx.doi.org/10.1016/j.pepi.2006.05.009.
Gilbert, F., Dziewonski, A.M., 1975. An application of normal mode theory to the retrieval of structural parameters and source mechanisms from seismic spectra. Philos. Trans. R. Soc. London A 278, 187–269.
Golombek, M.P., 2002. A revision of Mars seismicity from surface faulting, Lunar Planet. Sci. Conf. XXXIII, Abstract #1244.
Golombek, M.P., Banerdt, W.B., Tanaka, K.L., Tralli, D.M., 1992. A prediction of Mars seismicity from surface faulting. Science 258, 979–981.
Husen, S., Hardebeck, J., 2010. Earthquake Location Accuracy, Community Online Resource for Statistical Seismicity Analysis. http://dx.doi.org/10.5078/corssa-55815573. Available at: <http://www.corssa.org>.
Jeffreys, H., Bullen, K.E., 1940. Seismological Tables. British Association for the Advancement of Science, Burlington House, London.
Kanamori, H., 2005. Real-time seismology and earthquake damage mitigation. Annu. Rev. Earth Planet. Sci. 33, 195–214. http://dx.doi.org/10.1146/annurev.earth.33.092203.122626.
Kennett, B.L.N., Engdahl, E.R., 1991. Traveltimes for global earthquake location and phase identification. Geophys. J. Int. 105, 429–465.
Kennett, B.L.N., Engdahl, E.R., Buland, R., 1995. Constraints on seismic velocities in the Earth from traveltimes. Geophys. J. Int. 122, 108–124.
Khan, A., Connolly, J.A.D., 2008. Constraining the composition and thermal state of Mars from inversion of geophysical data. J. Geophys. Res. (Planets) 113, 7003.
Khan, A., Mosegaard, K., 2002. An inquiry into the lunar interior – a nonlinear inversion of the Apollo seismic data. J. Geophys. Res. 107. http://dx.doi.org/10.1029/ 2001JE001658.
Khan, A., van Driel, M., Böse, M., Giardini, D., Ceylan, S., Yan, J., Clinton, J., Euchner, F., Lognonné, P., Murdoch, N., Mimoun, D., Panning, M., Knapmeyer, M., Banerdt, W.B., 2016. Single-station and single-event marsquake location and inversion for structure using synthetic Martian waveforms. Phys. Earth Planet Int. 258 (28–42), 2016. http://dx.doi.org/10.1016/j.pepi.2016.05.017.
Knapmeyer, M., Oberst, J., Hauber, E., Wählisch, M., Deuchler, C., Wagner, R., 2006. Working models for spatial distribution and level of Mars' seismicity. J. Geophys. Res. 111, E11006. http://dx.doi.org/10.1029/2006JE002708.
Larmat, C.M., Montagner, J.-P., Capdeville, Y., Banerdt, B., Lognonné, P., Vilotte, J.-P., 2008. Numerical assessment of the effects of the topography and the crustal thickness on the Martian seismograms using the coupled modal solution-spectral elements method. Icarus 196, 78–89. http://dx.doi.org/10.1016/j.icarus.2007.12.030.
Lognonné, P., Johnson, C., 2007. Planetary seismology. In: Schubert, G. (Ed.), Treatise on Geophysics, 10. Elsevier, pp. 69–122.
Lognonné, P., & Johnson C.L., 2015. Planetary seismology. In: Schubert G (ed) Treatise on Geophysics, 10, 2nd edn, Elsevier, Oxford, 65-120, http://dx.doi.org/10.1016/B978-0-444-53802-4.00167-6.
Lognonné, P., Kawamura, T., 2015. Impact seismology on terrestrial and giant planets. In: Tong, V.C.H., Garcia, R. (Eds.), Extraterrestrial Seismology. Cambridge Univ. Press, Cambridge, U.K., pp. 250–263. http://dx.doi.org/10.1017/CBO9781107300668.021. chap 18.
Lognonné, P., Pike, W.T., 2015. Planetary seismometry. In: Tong, V.C.H., Garcia, R. (Eds.), Extraterrestrial Seismology. Cambridge Univ. Press, Cambridge, U.K., pp. 36–48. http://dx.doi.org/10.1017/CBO9781107300668.006. chap 3.
Lognonné, P., Gagnepain-Beyneix, J., Chenet, H., 2003. A new seismic model of the Moon: implication in terms of structure, formation and evolution. Earth Plan Sci. Lett. 6637, 1–18. http://dx.doi.org/10.1016/S0012-821X(03)00172-9.
Lognonné, P., Le Feuvre, M., Johnson, C.L., Weber, R.C., 2009. Moon meteoritic seismic hum: steady state prediction. J. Geophys. Res. 114, E12003. http://dx.doi.org/10.1029/2008JE003294.
Lognonné, P., W. B. Banerdt, D. Giardini, U. Christensen, D. Mimoun, S. de Raucourt, A. Spiga, R. Garcia, A. Mocquet, M. Panning, E. Beucler, L. Boschi, W. Goetz, T. Pike, C. Johnson, R. Weber, M. Wieczorek, K. Larmat, N. Kobayashi, & Tromp, J., 2012. InSight and Single- Station Broadband Seismology: From Signal and Noise to Interior Structure Determination, in Lunar and Planetary Science Conference, Lunar and Planetary Inst. Technical Report, 43, p. 1983.
Magotra, N., Ahmed, N., Chael, E., 1987. Seismic event detection and source location using single-station (three-component) data. Bull. Seismol. Soc. Am. 77 (3), 958–971.
Mimoun, D., Lognonné, P., Banerdt, W.B., Hurst, K., Deraucourt, S., Gagnepain-Beyneix, J., Pike, T., Calcutt, S., Bierwirth, M., Roll, R., Zweifel, P., Mance, D., Robert, O., Nébut, T., Tillier, S., Laudet, P., Kerjean, L., Perez, R., Giardini, D., Christenssen, U., Garcia, R., 2012. The InSight SEIS Experiment. In: Lunar and Planetary Science Conference, Lunar and Planetary Inst. Technical Report, 43, p. 1493.
Mocquet, A., Menvielle, M., 2000. Complementarity of seismological and electromagnetic sounding methods for constraining the structure of the Martian mantle. Planet. Space Sci. 48, 1249–1260.
Morelli, A., Dziewonski, A.M., 1993. Body wave traveltimes and a spherically symmetric P- and S-wave velocity model. Geophys. J. Int. 112 (2), 178–194.
Murdoch, M., Mimoun, D., Lognonné, P.H., & SEIS Science Team, 2015a. Seis performance model environment document, Tech. rep., ISGH-SEIS-JF-ISAE-030.
Murdoch, M., Mimoun, D., Lognonné, P.H., & SEIS Science Team, 2015b. Seis performance budgets, Tech. rep., ISGH-SEIS-JF-ISAE-0010.
Nakamura, Y., 1977. Seismic energy transmission in an intensively scattering environment. J. Geophys. 43, 389–399.
Nakamura, Y., 2005. Farside deep moonquakes and deep interior of the Moon. J. Geophys. Res. 110, E01001. http://dx.doi.org/10.1029/2004JE002332.
Nimmo, F., Faul, U.H., 2013. Dissipation at tidal and seismic frequencies in a melt-free, anhydrous Mars. J. Geophys. Res. (Planets) 118, 2558–2569.
Nissen-Meyer, T., van Driel, M., Stähler, S.C., Hosseini, K., Hempel, S., Auer, L., Colombi, A., Fournier, A., 2014. AxiSEM: broadband 3-D seismic wavefields in axisymmetric media. Solid Earth 5, 425–445. http://dx.doi.org/10.5194/se-5-425-2014.
Nolet, G., 2008. A Breviary of Seismic Tomography: Imaging the Interior of the Earth and Sun. Cambridge University Press, Cambridge, UK.
Oberst, J., Nakamura, Y., 1991. A search for clustering among the meteoroid impacts detected by the Apollo lunar seismic network. Icarus 91, 315–325.
Panning, M.P., Beucler, E., Drilleau, M., Moquet, A., Lognonné, P., Banerdt, W.B., 2015. Verifying single-station seismic approaches using Earth-based data: preparation for data return from the InSight mission to Mars. Icarus 248, 230–242.
Peterson, J., 1993. Observation and modeling of seismic background noise. U.S. Geol. Surv. Tech. Rept., 93-322, p. 94.
Phillips, R.J., 1991. Expected rates of Marsquakes. Scientific Rationale and Requirements for a Global Seismic Network on Mars, LPI Tech. Rep. 91-02 LPI/TR-91-02. Lunar and Planet. Inst., Houston, Tex, pp. 35–38.
Rivoldini, A., Van Hoolst, T., Verhoeven, O., Mocquet, A., Dehant, V., 2011. Geodesy constraints on the interior structure and composition of Mars. Icarus 213, 451–472.
Romanowicz B., 2002. Inversion of surface waves: a review, *IASPEI Handbook* (W. Lee Editor), Volume I.
Schwartz, S.Y., Thorne, L., 1987. Effects of off great-circle propagation on the phase of long-period surface waves. Geophys. J. R. Astron. Soc. 91 (1), 143–154. http://dx.doi.org/10.1111/j.1365-246X.1987.tb05217.x.
Selby, N.D., 2001. Association of Rayleigh waves using back azimuth measurements: application to test ban verification. Bull. Seismol. Soc. Am. 91, 580–593.
Smith, D.E. et al., 2001. Mars Orbiter laser altimeter: experiment summary after the first year of global mapping of Mars. J. Geophys. Res. 106, 23689–23722.
Sohl, F., Spohn, T., 1997. The interior structure of Mars: implications from SNC meteorites. J. Geophys. Res. 102, 1613–1635.
Solomon, S.C., Aharonson, O., Aurnou, J.M., Banerdt, W.B., Carr, M.H., Dombard, A.J., Frey, H.V., Golombek, M.P., Hauck, S.A., Head, J.W., Jakosky, B.M., Johnson, C.L., McGovern, P.J., Neumann, G.A., Phillips, R.J., Smith, D.E., Zuber, M.T., 2005. New perspectives on ancient Mars. Science 307 (5713), 1214–1220.
Stachnik, J.C., Sheehan, A.F., Zietlow, D.W., Yang, Z., Collins, J., Ferris, A., 2012. Determination of New Zealand ocean bottom seismometer orientation via Rayleigh-wave polarization. Seismol. Res. Lett. 83 (4), 704–713. http://dx.doi.org/10.1785/0220110128.
Teanby, N.A., Wookey, J., 2011. Seismic detection of meteorite impacts on Mars. Phys. Earth Planet. Inter. 186, 70–80.
van Driel, M., Krischer, L., Stähler, S.C., Hosseini, K., Nissen-Meyer, T., 2015. Instaseis: instant global seismograms based on a broadband waveform database. Solid Earth 6 (2), 701–717. http://dx.doi.org/10.5194/se-6-701-2015.
Verhoeven, O., Rivoldini, A., Vacher, P., Mocquet, A., Choblet, G., Menvielle, M., Dehant, V., Van Hoolst, T., Sleewaegen, J., Barriot, J.-P., Lognonné, P., 2005.

Interior structure of terrestrial planets: modeling Mars' mantle and its electromagnetic, geodetic, and seismic properties. J. Geophys. Res. (Planets) 110, 4009.
Walck, M.C., Chael, E.P., 1991. Optimal back azimuth estimation for three-component recordings of regional seismic events. Bull. Seismol. Soc. Am. 81 (2), 643–666.
Weber, M., Davis, J.P., 1990. Evidence of a laterally variable lower mantle structure from P- and S-waves. Geophys. J. Int. 102 (1), 231–255.
Wessel, P., Smith, W.H.F., Scharroo, R., Luis, J.F., Wobbe, F., 2013. Generic mapping tools: improved version released. EOS Trans. AGU 94, 409–410.
Zharkov, V.N., Gudkova, T.V., 2005. Construction of Martian interior model. Sol. Syst. Res. 39, 343–373.
Zhong, S.J., Zuber, M.T., 2001. Degree-1 mantle convection and the crustal dichotomy on Mars. Earth Planet. Sci. Lett. 189 (1–2), 75–84.